urbisphere-Berlin campaign: investigating multi-scale urban impacts on the atmospheric boundary layer

Fenner, D., Christen, A., Grimmond, S. ORCID: https://orcid.org/0000-0002-3166-9415, Meier, F., Morrison, W., Zeeman, M., Barlow, J., Birkmann, J., Blunn, L., Chrysoulakis, N., Clements, M., Glazer, R., Hertwig, D. ORCID: https://orcid.org/0000-0002-2483-2675, Kotthaus, S., König, K., Looschelders, D., Mitraka, Z., Poursanidis, D., Tsirantonakis, D., Bechtel, B., Benjamin, K., Beyrich, F., Briegel, F., Feigel, G., Gertsen, C., Iqbal, N., Kittner, J., Lean, H., Liu, Y., Luo, Z. ORCID: https://orcid.org/0000-0002-2082-3958, McGrory, M., Metzger, S., Paskin, M., Ravan, M., Ruhtz, T., Saunders, B., Scherer, D., Smith, S. T. ORCID: https://orcid.org/0000-0002-5053-4639, Stretton, M. ORCID: https://orcid.org/0000-0002-1444-5735, Trachte, K. and Van Hove, M. (2024) urbisphere-Berlin campaign: investigating multi-scale urban impacts on the atmospheric boundary layer. Bulletin of the American Meteorological Society, 105 (10). E1929-E1961. ISSN 1520-0477 doi: 10.1175/BAMS-D-23-0030.1 Available at https://centaur.reading.ac.uk/117568/

BAMS Article

urbisphere-Berlin Campaign: Investigating Multiscale Urban Impacts on the Atmospheric Boundary Layer

Daniel Fenner,[a] Andreas Christen,[a] Sue Grimmond,[b] Fred Meier,[c] William Morrison,[a,b] Matthias Zeeman,[a] Janet Barlow,[b] Jörn Birkmann,[d] Lewis Blunn,[e] Nektarios Chrysoulakis,[f] Matthew Clements,[b] Russell Glazer,[b] Denise Hertwig,[b] Simone Kotthaus,[g] Kai König,[a] Dana Looschelders,[a] Zina Mitraka,[f] Dimitris Poursanidis,[f] Dimitris Tsirantonakis,[f] Benjamin Bechtel,[h] Kit Benjamin,[b] Frank Beyrich,[i] Ferdinand Briegel,[a] Gregor Feigel,[a] Carlotta Gertsen,[a] Nimra Iqbal,[d] Jonas Kittner,[h] Humphrey Lean,[e] Yiqing Liu,[j] Zhiwen Luo,[k] Megan McGrory,[b] Swen Metzger,[a,l] Matthew Paskin,[b] Marvin Ravan,[d] Thomas Ruhtz,[m] Bethany Saunders,[b] Dieter Scherer,[c] Stefan Thor Smith,[j] Megan Stretton,[b] Katja Trachte,[n] and Melania Van Hove[o]

KEYWORDS:
Atmosphere-land interaction;
Boundary layer;
Instrumentation/ sensors;
Lidars/Lidar observations;
Numerical weather prediction/ forecasting;
Urban meteorology

ABSTRACT: For next-generation weather and climate numerical models to resolve cities, both higher spatial resolution and subgrid parameterizations of urban canopy–atmosphere processes are required. The key is to better understand intraurban variability and urban–rural differences in atmospheric boundary layer (ABL) dynamics. This includes upwind–downwind effects due to cities' influences on the atmosphere beyond their boundaries. To address these aspects, a network of >25 ground-based remote sensing sites was designed for the Berlin region (Germany), considering city form, function, and typical weather conditions. This allows investigation of how different urban densities and human activities impact ABL dynamics. As part of the interdisciplinary European Research Council Grant *urbisphere*, the network was operated from autumn 2021 to autumn 2022. Here, we provide an overview of the scientific aims, campaign setup, and results from 2 days, highlighting multiscale urban impacts on the atmosphere in combination with high-resolution numerical modeling at 100-m grid spacing. During a spring day, the analyses show systematic upwind-city-downwind effects in ABL heights, largely driven by urban–rural differences in surface heat fluxes. During a heatwave day, ABL height is remarkably deep, yet spatial differences in ABL heights are less pronounced due to regionally dry soil conditions, resulting in similar observed surface heat fluxes. Our modeling results provide further insights into ABL characteristics not resolved by the observation network, highlighting synergies between both approaches. Our data and findings will support modeling to help deliver services to a wider community from citizens to those managing health, energy, transport, land use, and other city infrastructure and operations.

DOI: 10.1175/BAMS-D-23-0030.1
Corresponding author: Daniel Fenner, d.fenner@tu-berlin.de
Supplemental information related to this paper is available at the Journals Online web-site: https://doi.org/10.1175/BAMS-D-23-0030.s1.

Manuscript received 16 February 2023, in final form 30 May 2024, accepted 20 July 2024

SIGNIFICANCE STATEMENT: A yearlong field campaign with a dense and systematic network of sites provides comprehensive measurements of the atmospheric boundary layer to gain deep knowledge of urban–rural and intraurban variability of surface–atmosphere exchanges. Understanding these is of high relevance for developing next-generation numerical weather prediction and climate models. We showcase the campaign and highlight synergies between ground-based and satellite observations and high-resolution numerical weather prediction modeling on two example days. Our findings show multiscale interactions between city and atmosphere, including urban-induced effects beyond the city's boundaries ("urban plume") and urban impacts under heatwave conditions. These results are important for developing dynamic modeling frameworks, which will help in delivering services to make cities more resilient.

AFFILIATIONS: [a] Chair of Environmental Meteorology, University of Freiburg, Freiburg, Germany; [b] Department of Meteorology, University of Reading, Reading, United Kingdom; [c] Chair of Climatology, Technische Universität Berlin, Berlin, Germany; [d] Institute of Spatial and Regional Planning, University of Stuttgart, Stuttgart, Germany; [e] Met Office@Reading, Reading, United Kingdom; [f] Remote Sensing Lab, Foundation for Research and Technology—Hellas, Heraklion, Greece; [g] Laboratoire de Météorologie Dynamique, École Polytechnique, Palaiseau, France; [h] Bochum Urban Climate Lab, Ruhr University Bochum, Bochum, Germany; [i] Deutscher Wetterdienst, Tauche—OT Lindenberg, Germany; [j] School of Built Environment, University of Reading, Reading, United Kingdom; [k] Welsh School of Architecture, Cardiff University, Cardiff, United Kingdom; [l] ResearchConcepts Io GmbH, Freiburg, Germany; [m] Radiation and Remote Sensing, Freie Universität Berlin, Berlin, Germany; [n] Chair of Atmospheric processes, Brandenburg University of Technology, Cottbus, Germany; [o] Institute Pierre Simon Laplace, École Polytechnique, Palaiseau, France

1. Introduction

Urban areas are increasing in population and spatial extent globally, and climate change risks to cities will rise rapidly with future global warming (Birkmann et al. 2016; IPCC 2023). This requires rapid responses to environmental extremes that impact not only the socioeconomic well-being of urban citizens but also the cascading effects in their country and/or region (Baklanov et al. 2018). Recognizing the demand for timely and comprehensive information on environmental extremes (WMO 2019), integrated urban services (IUS) are starting to be delivered, aided by increasing computer resources that enable high-resolution modeling (Loridan et al. 2013; Ronda et al. 2017; Lean et al. 2019, 2022). These IUS will help with managing cities both now and in the future to become more sustainable and resilient for their residents and infrastructure (WMO 2019, 2021; Grimmond et al. 2020). Central to IUS development are synergistic activities across many disciplines such as meteorology, hydrology, and air quality to ensure dynamic interactions are captured in models. This can help inform decisions in cities across the many critical space and time scales (Joe et al. 2021) using multiple data sources (Chrysoulakis et al. 2023).

Fundamental to achieving this is understanding and skillfully modeling surface–atmosphere exchanges and atmospheric boundary layer (ABL; Table 1) dynamics across metropolitan regions at high spatiotemporal resolutions. Urban areas are typically monitored with sparse observational networks (Grimmond et al. 2010; Muller et al. 2013) relative to the complexity and variability of urban form and function (e.g., Stewart and Oke 2012). Thanks to new instrument technologies (Foken 2021), higher-resolution satellite and airborne observations (Toth and Jóźków 2016; Wang et al. 2022; Storch et al. 2023;

Zheng et al. 2023; Zhong et al. 2023), high-resolution dynamical modeling for numerical weather prediction (NWP; Lean et al. 2019; Hall et al. 2024), and climate projections that account for cities (Masson et al. 2020; Ban et al. 2021), it has become evident that both urban form and function (i.e., people's behavior) need to be addressed (Barlow et al. 2017; Ching et al. 2018).

Table 1. List of abbreviations and variables.

Abbreviation	Description
AOD	Aerosol optical depth
ABL	Atmospheric boundary layer
BLH	ABL height
AGL	Above ground level
ALC	Automatic lidar and ceilometer
CO_2	Carbon dioxide
DWL	Doppler-wind lidar
EC	Eddy covariance
IUS	Integrated urban services
LAS	Large-aperture scintillometer
LST	Land surface temperature
MH	Mixing height (turbulence based)
MLH	Mixed-layer height (aerosol-concentration based)
NBL	Nocturnal ABL
NO_2	Nitrogen dioxide
NWP	Numerical weather prediction
Q^*	Net all-wave radiation
Q_E	Turbulent latent heat flux
Q_H	Turbulent sensible heat flux
T_{air}	Air temperature
UHI	Urban heat island

Past urban ABL studies (e.g., Oke and East 1971; Hildebrand and Ackerman 1984; Wood et al. 2013; Kotthaus and Grimmond 2018b; Zeeman et al. 2022), reviews (e.g., Fernando 2010; Barlow 2014), and large field campaigns [e.g., METROMEX (Changnon et al. 1971), URBAN 2000 (Allwine et al. 2002), BUBBLE (Rotach et al. 2005), UBL/CLU ESCOMPTE (Mestayer et al. 2005), JU2003 (Allwine and Leach 2007), CAPITOUL (Masson et al. 2008), ClearfLo (Bohnenstengel et al. 2015), SURF-2015 (Huang et al. 2017), and APHH-Beijing (Shi et al. 2019)] provide a wide range of insights into city–atmosphere interactions. However, short campaigns prevent seasonal variability from being explored. Furthermore, sensor networks are rarely extensive or systematically deployed to allow intraurban and urban–rural ABL variability or urban impacts on the ABL beyond city boundaries (e.g., Lowry 1977) to be explored.

Recognizing the advancements and challenges outlined above, the European Research Council-funded Synergy Grant *urbisphere* aims at transforming our understanding of urban–rural and intraurban variability in the three-dimensional nature of urban–atmosphere exchanges via fluxes of heat or moisture and resulting impacts on ABL characteristics. Here, we present the first major *urbisphere* field campaign. This is undertaken in the Berlin region in Germany (1 October 2021–30 September 2022) to investigate how the city modifies ABL characteristics on diurnal to annual time scales and at neighborhood (local, 10^2–10^4 m) to regional (10^1–10^3 km) spatial scales (Fig. 1). The latter allows the urban area to be put in context with its surrounding rural areas, both upwind and downwind of the city. At the neighborhood scale, spatial differences arising from differences in urban form and function determine intraurban heterogeneity (see "Urban form and human-activity cycles" sidebar). Additional *urbisphere* campaigns are being carried out in other cities, e.g., Paris, France, and Bristol, United Kingdom.

The goal of this paper is to showcase the potential of combining a systematic dense observation network of (near-)surface variables with ground-based remote sensing of ABL dynamics, satellite observations, and NWP modeling, to explore feedback mechanisms between cities, their surroundings, and the overlying atmosphere at different scales (Fig. 1). We use two case-study days to highlight the diverse and dynamic nature of surface–atmosphere interactions. Both days demonstrate the value of our multiscale approach and the potential of these observations to enhance high-resolution NWP as part of developing IUS for cities and society.

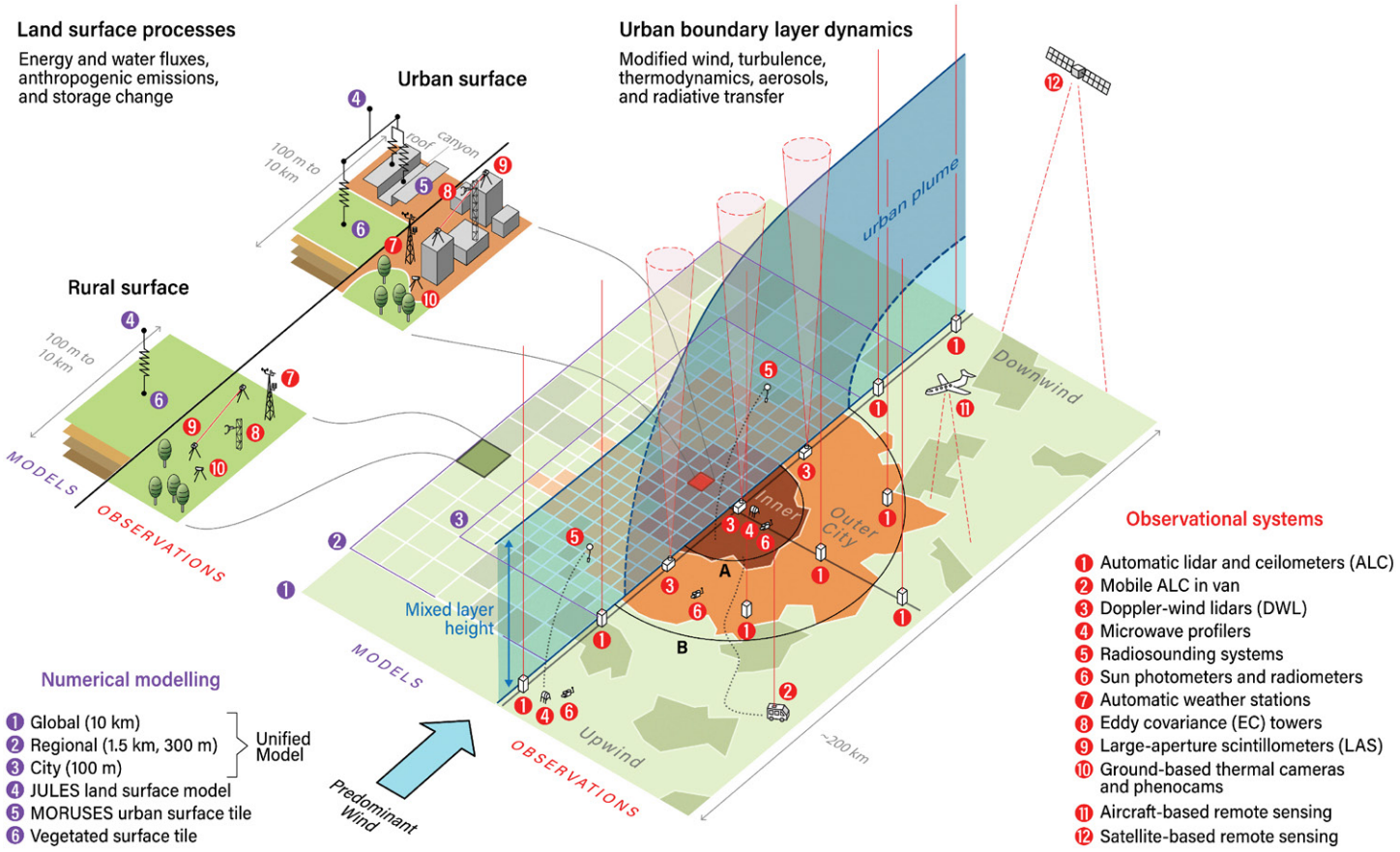

Fig. 1. Conceptual sketch of the integrated research design of *urbisphere*-Berlin combining systematic observations and numerical modeling, showing campaign measurement systems, modeling approach, processes addressed, and scales.

Urban form and human-activity cycles

Central to *urbisphere* is the dynamic nature of cities, manifested in interactions between the physical structure of the city (urban form) and human activities (function) which impact the magnitude and timing of anthropogenic emissions (e.g., heat and pollutants). Detailed *urbisphere* modeling combines human activity with building energy (e.g., Liu et al. 2022), transport (e.g., McGrory et al. 2024), and exposure of individuals to environmental stressors (e.g., Xie et al. 2023). Agent-based models capture the complex interplay of form and function to predict and diagnose their combined effects across relevant spatiotemporal scales (Capel-Timms et al. 2020; Liu et al. 2023; Hertwig et al. 2024).

The intraurban variability of function, such as measured by the ratio of nonresidential (NR) to residential (R) building volumes (Fig. SB1a), can vary between clustered and dispersed building uses. The degree of workplace (de)centralization (compared to residential) areas allows conclusions on functional networks (e.g., commuting patterns) and spatiotemporal variability of occupancy (daytime and nighttime populations). Urban function may change by time of day, day of week, month, season, or decade (e.g., reflecting social norms and governance), but is also impacted by weather (e.g., wet, hot, and modifying transport mode/route), behavior of occupants (e.g., how busy a place is), and demography as well as socioeconomic conditions.

To illustrate the impacts of human-activity cycles, we use measured carbon dioxide (CO_2) fluxes. Reduced weekend versus weekday CO_2 fluxes in winter 2021/22 show consistent impacts from typical work patterns influencing magnitude and timing of traffic emissions (Fig. SB1b). Site TUCC (Table 2) has larger weekend CO_2 flux reductions than site ROTH, linked to many NR university and office buildings plus major traffic arteries (Fig. SB1c). Particle number flux measurements are consistent with this (Straaten and Weber 2021). However, the high use of district heating near TUCC rather than individual gas boilers used by the single-family houses near ROTH (Fig. SB1d) caused the difference in the CO_2 fluxes observed between these two sites. Contributing is the COVID-19–related reduced human activity near TUCC during winter 2021/22 from regulations requiring many workers to be home-based, reducing emission fluxes (Nicolini et al. 2022; Straaten et al. 2022).

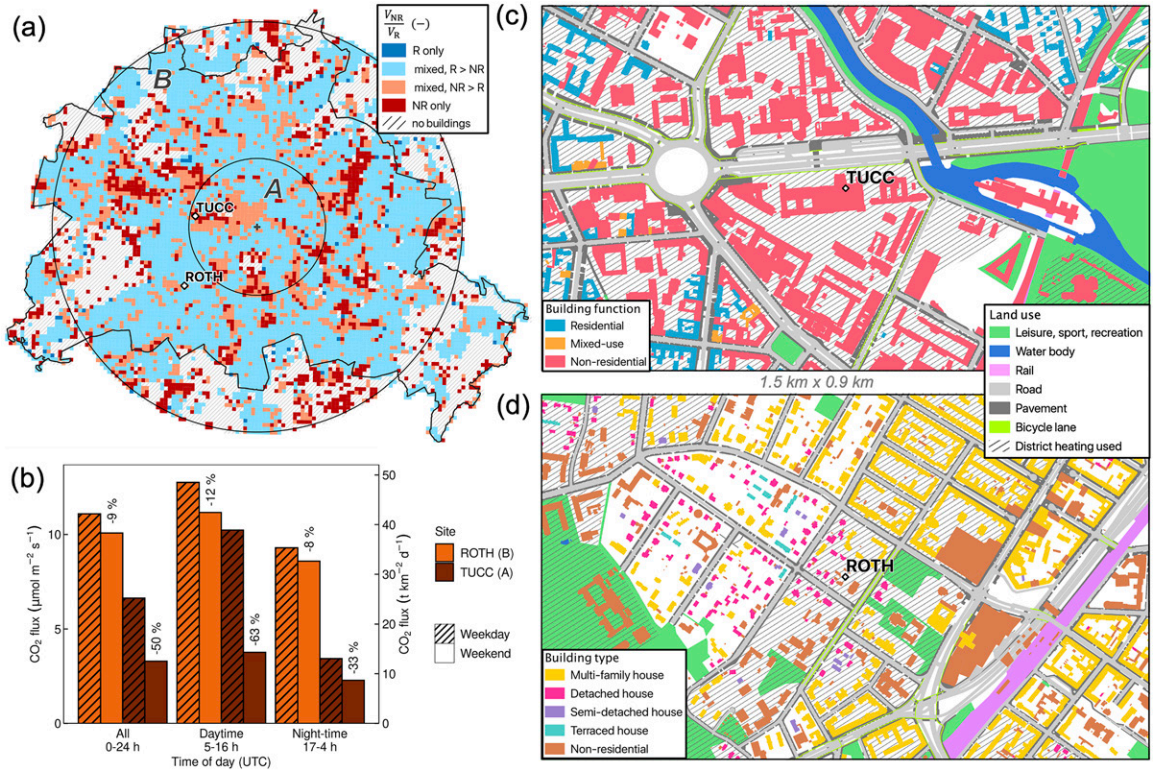

FIG. SB1. Spatial and temporal variability of urban form and function in Berlin: (a) ratio of NR to R building volume V_{NR}/V_R for 300-m grid cells and CO_2 flux sites (diamond); (b) weekdays and weekends (% differences shown) winter (DJF, 2021/22) mean CO_2 fluxes at TUCC (ring A) and ROTH (B). For both sites, the main DJF wind sector is from south to northwest. Land use and building footprints around the flux sites showing (c) building function at TUCC and (d) residential building form typologies at ROTH (data: appendix H).

Spatial variation and temporal evolution of urban form are determined by scales of governance (e.g., national regulations and local city planning) and socioeconomic factors at the household or community level (e.g., building refurbishment and neighborhood gentrification). Activities and living circumstances of individuals at the building scale are surveyed nationally (e.g., time-use surveys, as used in agent-based models; Capel-Timms et al. 2020; Hertwig et al. 2024) and in *urbisphere*'s own stratified samples (Iqbal et al. 2024), providing a snapshot in time of aspects of people's behavior and its influencing factors (e.g., choice of energy use and response to weather and climate hazards). The analysis of urban form and function, including aspects of exposure to climatic hazards and human vulnerability, allows better assessment of dynamics of risks within cities.

2. Conceptual background of network design

With the Berlin metropolitan region distant from other large urban areas (Figs. 2 and 3) and far from the sea in flat topography, it provides ideal conditions for studying urban effects in temperate midlatitude cities. The region has been subject to diverse (urban) atmospheric studies for over a century (e.g., Perlewitz 1890; Horbert et al. 1984; Hupfer and Chmielewski 1990; Geiß et al. 2017; Schneider et al. 2022), including recent observation campaigns, mostly focusing on air quality and/or model evaluation (e.g., Becker et al. 2002; Bonn et al. 2016; Scherer et al. 2019a,b; Hohenegger et al. 2023). A wide range of high-quality, ongoing observations are undertaken by several institutions in the region, complementing the *urbisphere*-Berlin network deployed during 2021/22.

To achieve *urbisphere*'s multicity goals consistently, the sensor network is designed to capture spatial variability within the region and city, while ensuring both urban form

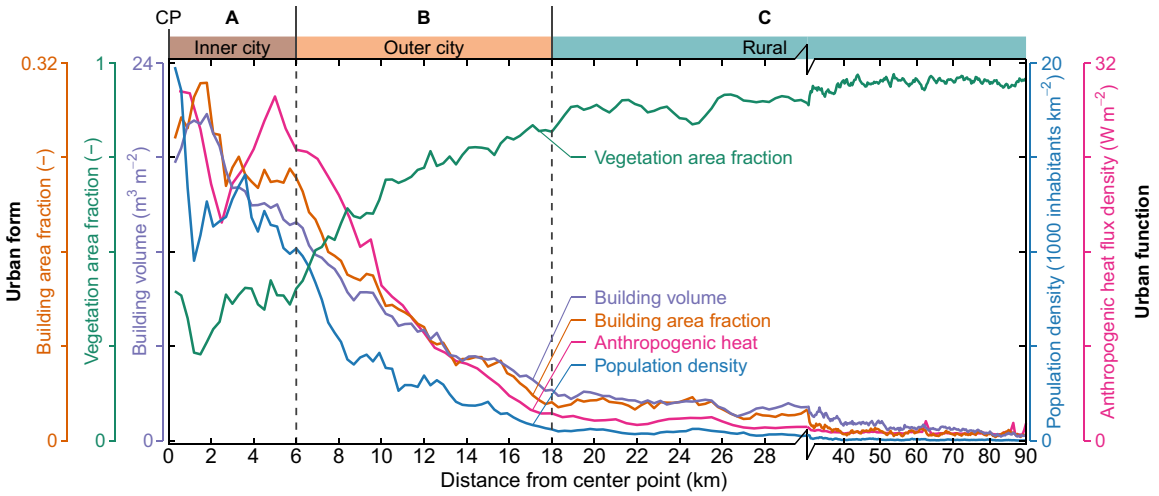

Fig. 2. Five mean characteristics (color) of urban form and function of the Berlin region by distance from CP (52.504 936°N, 13.408 125°E) analyzed with 300-m annuli and the derived ring boundaries (dashed vertical lines). Note that *x* axis breaks at 30 km. Sources and analysis given in appendix A.

and function are represented. As urban atmospheric effects are not limited to the extent of the city itself but go beyond city boundaries and plan area (e.g., Lowry 1977; Bassett et al. 2016; Lorenz et al. 2019), the design allows upwind-city-downwind effects to be captured by observations and modeling. Our goal is to compare both urban–rural and intraurban scales for an individual city in a framework that also allows global intercity comparisons.

In view of this, our study utilizes three rings surrounding a city center point (CP), based on urban form and function characteristics. The determined center point (52.504 936°N, 13.408 125°E) and rings for Berlin (Fig. 2 and Fig. SM1.1 in the online supplemental material) neither follow administrative boundaries nor perfectly capture the shape of the built-up area (Fig. SB1a). Although the proposed framework and workflow require city-specific adaptation, it enables city characterization and reporting results in a more objective manner. For Berlin, the inner-city (A), outer-city (B), and rural (C) rings have radii of 6, 18, and 90 km, respectively (Fig. 2, Fig. SM1.1, and appendix A). We use the three rings to (a) stratify sensor deployment between areas; (b) identify modeling domain extents, with their required nesting boundary conditions buffers (Fig. 3a); and (c) give a generically repeatable method for comparing cities in a general sense (e.g., fraction of area covered by buildings, vegetation, and population density).

The observational network design also needs to consider the different sensor types and their underlying principles impacting the source areas, i.e., areas influencing the observed variable at the sensor location during a measurement period (Fig. 1). Some sensors have large dynamic fields of view, such as Doppler wind lidars (DWLs) programmed to address multiple objectives [e.g., wind profiles and turbulence-based mixing height (MH)], while large-aperture scintillometers (LASs) require turbulent flux footprint analysis along their path (Saunders et al. 2024) to know what of Berlin's predominant urban form and function types are sampled.

3. Methods

a. Sensors and observational network. The diversity of sensors deployed (Table 2) complements long-term past and ongoing observations including tower-based energy-balance fluxes (e.g., Vulova et al. 2021), satellite-based land surface temperature [LST; e.g., Moderate Resolution Imaging Spectroradiometer (MODIS); Wan et al. 2021], and automatic

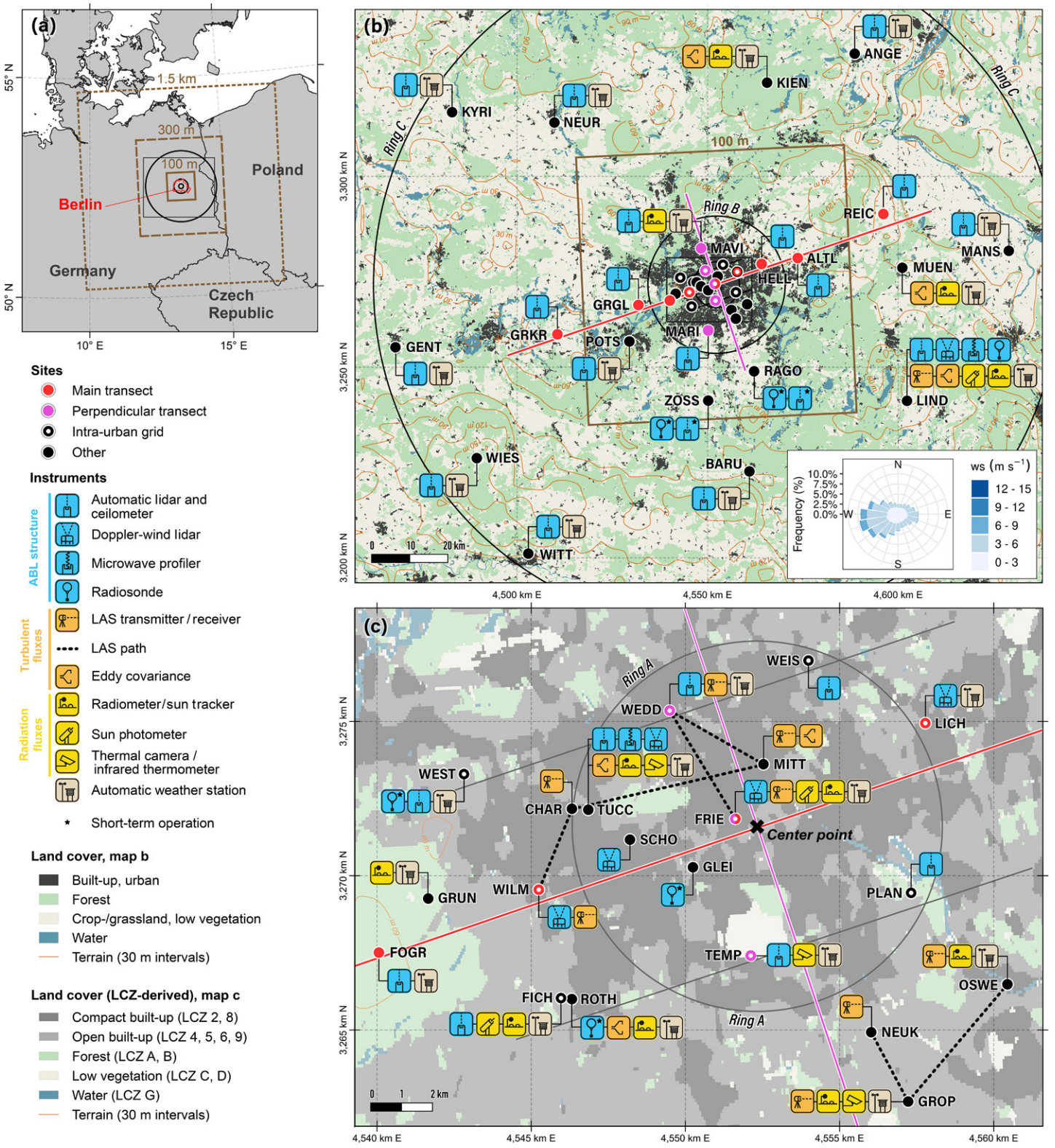

FIG. 3. *urbisphere*-Berlin study region: (a) location in Europe with NWP model domains (brown rectangles) and their horizontal gridcell resolution, and *urbisphere* rings (black circles), with Berlin administrative boundary (red) and extent of (b) (black rectangle); (b) observation sites with instruments (symbols and names) with *urbisphere* rings A (inner city, radius: 6 km), B (outer city, radius: 18 km), and C (rural, radius: 90 km), sensor transects (solid lines), inner modeling domain (brown rectangle), land cover (Buchhorn et al. 2020), and terrain contours, wind rose [1991–2020, derived from ERA5 6-h 10-m wind components (Hersbach et al. 2023), spatial mean for 12.5°–14°E by 52°–53°N, ws—wind speed], and extent of (c) (black rectangle); and (c) inner-city observation sites with instruments, LAS paths (dashed lines), sensor transects (solid lines), land cover (derived from LCZs; Fenner et al. 2017), and terrain contours. Terrain data: European Environment Agency (EEA) (2016). Projection: Lambert azimuthal equal area. Datum: ETRS89-extended/Lambert azimuthal equal area (LAEA) Europe.

Table 2. ***urbisphere*-Berlin measurement sites and sensors operated on the ground (G) or roof (at given height) at given elevation MSL. Listed sites are used in the campaign, but others exist in the region. Instruments include automatic lidar and ceilometers (*), DWL (+), radiosonde (◊), microwave profilers (∞), LAS (#) consisting of a transmitter (Tx) and receiver (Rx), EC (⁜), radiometers (°; sun tracker includes CHP1, CG1/CGR4, and CM21), thermal infrared sensors (╬), sun photometer (↑), and AWS with at least air temperature and humidity measurements. Start date (‡) earlier than 1 Oct 2021 and end date (‡) ongoing, but all may have gaps. Operators are *urbisphere*/University of Freiburg (UFR) [some also University of Reading (UR)], Deutscher Wetterdienst (DWD), Technische Universität Berlin (TUB), Freie Universität Berlin (FUB), Landesbetrieb Forst Brandenburg (LFB), Brandenburg University of Technology (BTU), FUTURE/UR, and HTW Berlin–University of Applied Sciences (HTW). Supplemental material 2 provides more site, sensor, and data acquisition information, and data processing details are given in appendixes.**

Site code	Site name	Latitude (°N)	Longitude (°E)	Ring	Elevation (m; MSL)	Sensor height (m)	ABL structure	Turbulent fluxes	Radiation fluxes	Standard meteorology	Date		Operator
											Start	End	
ALTL	Altlandsberg	52.557283	13.727988	C	57.5	G	CL61*				11 Nov 2021	6 Jul 2022	UFR
ANGE	Angermünde	53.031631	13.990849	C	54.0	G	CHM15k*			AWS	‡	‡	DWD
BARU	Baruth	52.061375	13.499704	C	54.9	G	CHM15k*			AWS	‡	22 Jun 2022	DWD
CHAR	Charlottenburg	52.512745	13.320066	B	33.8	77.8		BLS450:Tx# BLS2000:Tx#			27 Aug 2021	12 Oct 2022	UFR, TUB
FICH	Fichtenberg	52.457794	13.310898	B	66.6	10.4	CHM15k*		CM21°, CSD1°, CE318-T↑	AWS	‡	‡	FUB
FOGR	Forest Grunewald	52.473253	13.225099	B	55.9	G	CHM15k*			AWS	‡	‡	TUB
FRIE	Friedrichstadt	52.507556	13.397881	A	34.1	73.7	StreamLine+	BLS2000:Rx#	Sun Tracker°, CE318-T↑	AWS	15 Jul 2021	6 Oct 2022	UFR
GENT	Genthin	52.387542	12.160061	C	34.9	G	CHM15k*			AWS	‡	‡	DWD
GLEI	Gleisdreieck	52.494010	13.376607	A	37.5	G	Windsond◊				4 Aug 2022	11 Aug 2022	UFR
GRGL	Gross Glienicke	52.465286	13.102737	C	44.0	3	CL61*				10 Sep 2021	10 Oct 2022	UFR
GRKR	Gross Kreutz	52.403896	12.785645	C	31.3	G	CL31*				1 Sep 2021	14 Oct 2022	UFR
GROP	Gropiusstadt	52.422949	13.473843	B	43.8	80.1		BLS450:Rx# BLS2000:Rx#	Sun Tracker°, IR120╬, PI-160╬	AWS	26 Jan 2022	20 Oct 2022	UFR, UR
GRUN	Grunewald	52.488500	13.249440	B	55.2	4.6			Sun Tracker°	AWS	10 May 2022	17 Oct 2022	UFR
HELL	Hellersdorf	52.548064	13.585989	B	51.0	G	CL61*				13 Sep 2021	7 Oct 2022	UFR
KIEN	Kienhorst	52.973419	13.643776	C	78.1	G		R3-50‡ LI-7500‡	CNR4°	AWS	‡	‡	LFB
KYRI	Kyritz	52.936310	12.409355	C	40.2	G	CHM15k*			AWS	‡	‡	DWD
LICH	Lichtenberg	52.532620	13.490361	B	60.3	G	StreamLine+			AWS	25 Aug 2021	4 Oct 2022	UFR
LIND	Lindenberg	52.208532	14.118009	C	97.7	G	CHM15k*, StreamLine+, HATPRO∞, RS41-SGP◊	BLS900#, USA-1‡, LI-7500‡	CGR4°, CM22°, CE318-T↑	AWS	‡	‡	DWD
MANS	Manschnow	52.546856	14.545148	C	12.0	G	CHM15k*			AWS	‡	‡	DWD
MARI	Marienfelde	52.398415	13.368076	B	46.9	2.5	CL31*				2 Sep 2021	13 Oct 2022	UFR
MAVI	Märkisches Viertel	52.592138	13.355699	B	47.8	23.3	CL31*		Sun Tracker°	AWS	23 Jun 2022	21 Oct 2022	UFR
MITT	Mitte	52.523081	13.412517	A	37.1	123.4		BLS450:Rx# BLS2000:Rx# IRGASON‡			31 Aug 2021	11 Oct 2022	UFR
MUEN	Müncheberg	52.521694	14.129849	C	63.6	G		WindMaster Pro‡ LI-7500‡	NR01°	AWS	10 Jun 2022	19 Sep 2022	BTU
NEUK	Neukölln	52.443652	13.457817	B	35.9	24.9		BLS450:Tx# BLS900:Tx#			23 Nov 2021	19 Oct 2022	UFR
NEUR	Neuruppin	52.903729	12.807121	C	38.4	G	CHM15k*			AWS	‡	‡	DWD
OSWE	Oberschöneweide	52.455712	13.524017	B	34.5	27.6		BLS2000:Tx#	SHP1°, CMP11°, SMP21°	AWS	23 Nov 2021	19 Oct 2022	HTW, UFR
PLAN	Plänterwald	52.483590	13.479983	A	35.0	11.4	CL31*				23 Sep 2021	4 Oct 2022	UFR

(*Continued*)

Table 2. (*Continued*).

Site code	Site name	Latitude (°N)	Longitude (°E)	Ring	Elevation (m; MSL)	Sensor height (m)	ABL structure	Turbulent fluxes	Radiation fluxes	Standard meteorology	Date		Operator
											Start	End	
POTS	Potsdam	52.381 108	13.062 117	C	80.8	G	CHM15k*		CG(R)4°, CM11°, CMP22°	AWS	‡	‡	DWD
REIC	Reichenow	52.650 763	14.067 637	C	70.9	4	CL31*				11 Nov 2021	7 Oct 2022	UFR
RAGO	Ragow	52.296 605	13.538 686	C	44.1	G	CL61*, Windsond◊			AWS	11 Aug 2022	11 Aug 2022	UFR
ROTH	Rothenburgstraße	52.457 257	13.315 781	B	46.4	G		IRGASON‡	CNR4°, SPN1°	AWS	‡	‡	TUB
SCHO	Schöneberg	52.502 927	13.347 332	A	35.2	54.4	StreamLine+				28 Jun 2022	5 Oct 2022	UR
TEMP	Tempelhof	52.467 502	13.402 222	A	47.9	G	CL61*/CL31*		IR120╬	AWS	20 Sep 2021	5 Oct 2022	DWD, UFR
TUCC	TUB Campus Charlottenburg	52.512 238	13.327 804	A	34.0	45.4	CHM15k*, StreamLine XR+, HATPRO∞	IRGASON‡	CNR4°, SPN1°, IR120╬	AWS	‡	‡	TUB
WEDD	Wedding	52.540 129	13.368 945	A	35.8	65.5	CL61*	BLS450:Tx# BLS2000:Tx#		AWS	26 Aug 2021	12 Oct 2022	UFR
WEIS	Weißensee	52.552 620	13.436 642	A	48.3	G	CL31*				21 Sep 2021	11 Oct 2022	UFR
WEST	Westend	52.524 105	13.269 433	B	55.7	G	CL31*			AWS	24 Sep 2021	14 Oct 2022	UFR
WIES	Wiesenburg	52.120 703	12.458 597	C	187.0	G	CHM15k*			AWS	‡	‡	DWD
WILM	Wilmersdorf	52.489 598	13.302 705	B	45.6	93.8	StreamLine XR+	BLS450:Rx#			8 Sep 2021	10 Oct 2022	UFR
WITT	Wittenberg	51.889 181	12.644 598	C	104.6	G	CHM15k*			AWS	‡	‡	DWD
ZOSS	Zossen	52.232 072	13.357 386	C	49.3	G	CL61*, Windsond◊			AWS	4 Aug 2022	4 Aug 2022	UFR

weather stations (AWSs) (e.g., Fenner et al. 2014; Langer et al. 2021). Many observations have multiple uses, including detailed process studies, model development and evaluation, as well as complementing other measurements (e.g., wind speed for LAS heat fluxes and radiosondes for LST retrieval from airborne and spaceborne sensors). In total, there are 41 sites, with nine inner-city (ring A, 0–6 km radius), 14 outer-city (ring B, 6–18 km radius), and 18 rural (ring C, 18–90 km) sites. All measurement sites are given a four-letter code (Table 2).

The ALC and DWL sensors form the core of the campaign network. The ALC sensors measure vertical profiles of attenuated backscatter, allowing cloud-base height, cloud cover, and aerosol-concentration-based mixed-layer height (MLH) to be determined (appendix B). Five ALC sensors also provide a linear depolarization ratio allowing aerosol shape to be inferred. The DWL sensors allow different scanning schemes (e.g., wind-profile scans and stare measurements) and measure profiles of attenuated backscatter, as well as the Doppler frequency shift of the laser signal. This enables deriving vertical and horizontal wind speed, wind direction, turbulence characteristics, and turbulence-based MH (appendix B). Our network design has a main transect of nine ALC and DWL sensors along the prevailing wind direction [west-southwest (WSW)] through the city center, covering the three rings including upwind and downwind rural areas to observe rural–urban–rural differences and urban plume effects (Figs. 1 and 3). Given the wind-direction variability, both parallel and perpendicular secondary transects are added (Figs. 3b,c). An intraurban grid of sensors allows for the intraurban variability of atmospheric conditions to be studied (Fig. 3c). With ten preexisting ALC sites in ring C, rural and urban areas can be compared.

Both LAS and eddy covariance (EC) sensors are used to obtain turbulent sensible heat fluxes between the surface and atmosphere (Q_H). To ensure the LAS beams are within the inertial sublayer, the transmitters and receivers for all six urban LAS paths (≤∼6 km; Fig. 3c) are mounted on tall buildings. The six EC sites (Table 2 and Fig. 3), also providing

other fluxes [e.g., latent heat (Q_E) and carbon dioxide (CO_2)], are located in the city center (MITT), medium-to-high density or inner-city park depending on wind direction (TUCC), suburban (ROTH), and three rural sites (grassland: LIND, orchard: MUEN, and pine forest: KIEN) (appendix C).

As downwelling longwave, shortwave, and spectral radiation sensors require minimal horizon obstructions, roof deployments are used (Table 2). To derive aerosol optical depth (AOD), three sun photometers (A: FRIE, B: FICH, and C: LIND) (Fig. 3) are used. Urban–rural and upwind-city-downwind analyses can use four sun trackers plus other radiation sites across the area. Four-component radiometers provide incoming/outgoing shortwave, longwave, and net all-wave radiation Q^* at five EC sites (Table 2 and appendix D). Thermal infrared sensors at three sites (GROP, TEMP, and TUCC) allow LST to be determined for different facets and materials. Six near-surface automatic weather stations complement existing sites (Table 2), as well as a dense network of crowdsourced weather stations (appendix F).

Two intensive observation periods (IOPs) in spring and summer 2022 include a van-mounted ALC (see "Mobile ALC deployment for detecting MLH at high spatial resolution" sidebar) and radiosonde launches (appendix E). During the summer IOP (1–12 August 2022), aircraft-mounted SatVu midinfrared and drone-mounted thermal infrared sensors are operated, providing LST at spatial resolutions between those of ground-based and satellite sensors. The latter include Sentinel-3, MODIS, Advanced Spaceborne Thermal Emission and Reflection Radiometer (ASTER), Ecosystem Spaceborne Thermal Radiometer Experiment on Space Station (ECOSTRESS), and Landsat overpasses (appendix G).

Comprehensive site, instrument, and campaign details (e.g., instrument regular maintenance) are provided in supplemental material 2. Central infrastructure gathers the data of all these network-connected systems (Zeeman et al. 2024). The infrastructure identifies and archives data by location, instrument model, and production level. Metadata details include operational sensors, deployment configurations, and maintenance. Online tools allow metadata editing, problem tracking, and data quality review. Dashboard apps (e.g., preview figures and recent file listings) facilitate data management and near-real-time monitoring through shared responsibilities. Subsequent data processing to level 2 products presented here is given in the appendixes. All times are coordinated universal time (UTC) and indicate interval ending.

Mobile ALC deployment for detecting MLH at high spatial resolution

Since mobile ALC deployments (e.g., Pal et al. 2012; Peng et al. 2017; Lamer et al. 2022) can enhance information about the horizontal spatial variability of MLH, we explore this in Berlin (Fig. SB2a) using a CL61 ALC observing attenuated backscatter and linear depolarization ratio. The latter provide information related to aerosol concentration and shape with a high signal-to-noise ratio (e.g., Inoue and Sato 2023). The quick-to-deploy mobile platform (Fig. SB2a) includes air temperature, humidity, and GPS location observations.

On 11 August 2022, the van was driven approximately perpendicular to the wind direction (Figs. SM1.9, SM1.10), from near the city center, across the city into the rural (~10 km, RAGO; Fig. 3b) surroundings southeast of Berlin, and back, during the morning transition. The cloud-free morning followed a clear night, with low easterly winds (105°, 2 m s^{-1} at 10 m AGL at TEMP, 0600–0700 UTC) with northeasterly flow above the mixing layer. The ALC data are complemented with concurrent radiosonde launches at both RAGO and an inner-city site (GLEI; Fig. 3c). Radiosonde profiles and derived inversion heights (Fig. SB2b) and ALC observations with derived MLH (Figs. SB2c,d) allow a detailed analysis of the vertical structure of the ABL.

Generally, observed attenuated backscatter and LDR are larger in the built-up areas compared to rural due to higher urban than rural aerosol emissions during the morning rush hour. At the inner-city site TEMP between 0600 and 0635 UTC, the MLH (200 m AGL) is 47% greater than at rural RAGO (136 m AGL). Radiosonde inversion heights also indicate a deeper urban ABL (GLEI 199 m AGL; RAGO 150 m AGL) and good agreement between both methods (appendixes B and E), similar to Lotteraner and Piringer (2016). The transect MLH decreases after leaving the built-up area at ~0600 UTC and sharply increases upon entering built-up areas from the countryside at ~0635 UTC (Figs. SB2c, SM1.9, SM1.10). The stationary inner-city ALC at TEMP during the same period shows an incremental increase in MLH (Fig. SB2c). A spike in both variables at ~0634 UTC (Figs. SB2c,d), extending up to the top of the ABL, may be related to exhaust gases of a departing airplane, when the van crossed the Berlin–Brandenburg airport flight path. Capturing such small-scale variations in aerosols and MLH at boundaries between different land covers is a defining feature of mobile measurements.

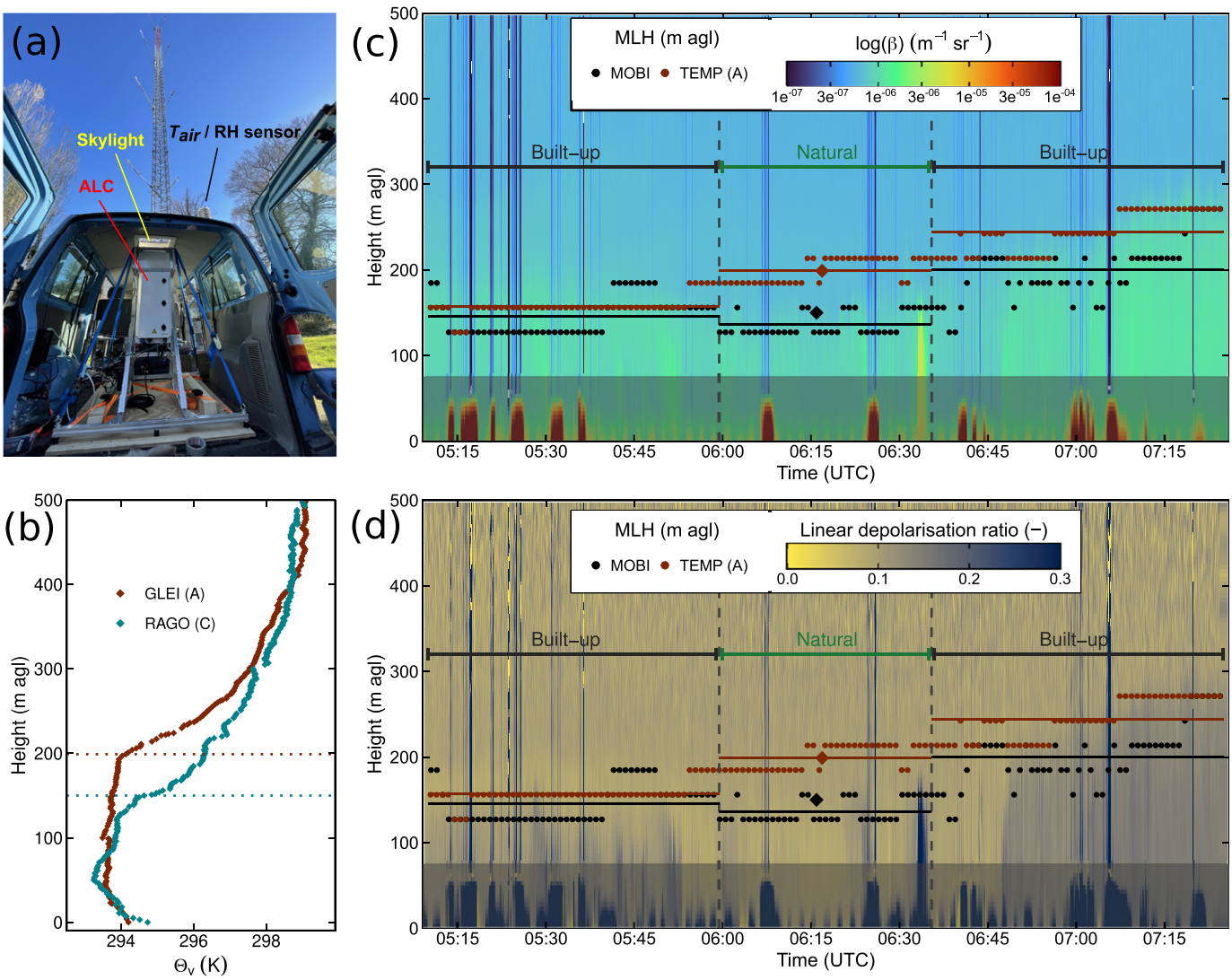

FIG. SB2. On 11 Aug 2022, the mobile system MOBI deployed with (a) CL61 ALC mounted in a van (shown at ROTH 40 m flux tower site), (b) radiosondes virtual potential temperature θ_v launched at 0615 UTC from inner-city (GLEI) and rural (RAGO) sites with ABL height (dotted line; appendix E), (c) MOBI CL61 attenuated backscatter β (colorbar) and MLH (points; appendix B) for both inner-city (TEMP) ALC and mobile (MOBI) ALC, with mean (horizontal line) between location (dashed vertical lines) and radiosonde ABL height [from (b), diamonds]. (d) As in (c), but with LDR (colorbar). (c) and (d) data <70 m AGL are not considered in MLH calculations (gray area) due to artifacts when the mobile ALC is below bridges, tree canopy or in tunnels.

b. NWP modeling. The Met Office Unified Model, version 13 (UM v13.0; Davies et al. 2005; Wood et al. 2014), is used to simulate the two case-study days. The one-way nested domains (1.5 km → 300 m → 100 m with 70 → 70 → 140 vertical layers, respectively; Fig. 3) are within the 10-km global UM model (Global Atmosphere v8.0 and Global Land v9.0 science configurations, updated from Walters et al. 2019), with each nest providing the boundary conditions. A 36-h simulation is undertaken starting at 1200 UTC on the day prior to the day of interest. Domain 2 with $O(300)$ m resolution encompasses all three campaign rings (Fig. 3a). The Regional Atmosphere and Land 3.1 (RAL3.1) science configuration used for the nested domains has physical scheme improvements post-RAL2 (Bush et al. 2023), with the primary modification being the integration of the tropical and midlatitude configurations, encompassing updates to cloud (Van Weverberg et al. 2021a,b) and microphysical (Field et al. 2023) parameterizations. Subgrid-scale turbulence is parameterized using

the Boutle et al. (2014) "scale-aware" method. The Joint UK Land Environment Simulator (JULES v7.0; Best et al. 2011; Clark et al. 2011; Walters et al. 2019) is used with the Met Office Reading Urban Surface Exchange Scheme (MORUSES) (Porson et al. 2010a,b; Bohnenstengel et al. 2011) option for the built form, which has two tiles (roof and street canyon; Fig. 1). The land-cover fraction data used are ESA Climate Change Initiative (CCI) version 1 (ESA 2017). Anthropogenic heat flux is prescribed as a constant monthly value that varies with urban fraction in a grid cell (Hertwig et al. 2020). Biases in modeled urban soil moisture have been found previously (e.g., Hertwig et al. 2020; Hall et al. 2024). Here, unrealistically large initial soil-moisture values in the built-up areas are replaced with the suburban and rural regional median for case-study day 2.

4. Results and discussion

We focus on two days to explore different aspects of the spatial variability of ABL conditions (urban, rural, and intraurban) that are relevant to operational NWP, provision of IUS, and long-term climate analyses:

1) Spring day at time of leaf emergence (18 April 2022, Easter Monday, public holiday): After a dry March 2022 (1.3 mm total, compared to 1991–2020 normal: 40.5 mm; site TEMP; DWD 2023a; and subsequent values), 1–17 April 2022 is wetter (28.5 mm, normal for April: 29.3 mm). After a cool morning (2.4°C 2 m air temperature T_{air}) on the nearly cloud-free day, afternoon T_{air} reaches 15.5°C in ring A, with a consistent northeasterly wind (Fig. SM1.4).
2) Summer day during a heatwave (4 August 2022, weekday): Like much of Europe, the Berlin area is dry, after below-normal (1991–2020) precipitation from May to July (86 mm, normal: 182.2 mm; DWD 2023a), with no rain in the eight days prior. The daily available soil-water capacity (22%; modeled loamy-sand soil, 0–0.6 m; DWD 2019) is substantially lower than the August normal [47.1%; available water capacity = 78 mm]. A strong heat alert warning was in force (3–4 August; DWD 2021), and maximum near-surface T_{air} = 37.3°C (TEMP) makes this the second-hottest day of 2022 and eighth-hottest day in the period 1991–2022 (DWD 2023a).

a. Case 1: Spring day with an urban plume. Following the spring equinox, increasing incoming shortwave radiation warms the surface and building walls, resulting in plant growth and changes in surface-energy-flux partitioning. On 18 April 2022, deciduous trees in the Berlin–Brandenburg area were mostly in a leaf-off state, with leaf emergence just beginning (e.g., Hanging Birch—18 April and European Beech—23 April; DWD 2022). With the leaf area index still low, much of the incoming radiation is released as Q_H at the surface (Kotthaus and Grimmond 2014). The 3D variability of urban form and function across cities (Fig. 2; see "Urban form and human-activity cycles" sidebar) results in local-scale differences in surface-energy-flux partitioning. The smaller observed albedo in the city (0.10, ROTH, B) compared to the rural grassland (0.22, LIND, C) results in a larger daytime Q^* in the city (Fig. 4a). Consistent results are modeled, but the model contrast between urban (rings A and B) and rural (ring C) sites is smaller, as the albedo differences are less (ring B: 0.13 and ring C: 0.15). Note the rings' modeled albedo includes different land-cover types, with forest albedo typically less than grassland as observed at LIND.

Evident from both LAS and EC observations (Fig. 4b), the absolute daytime peak Q_H is larger in both urban rings than in the rural areas. The EC and LAS Q_H data have good agreement at sites where both are measured (Fig. 4b; LIND), as reported previously (e.g., Mestayer et al. 2005; Ward et al. 2014). During the midday peak period (1000–1400 UTC), the total LAS Q_H is 59% greater for the three urban paths (rings A + B) than

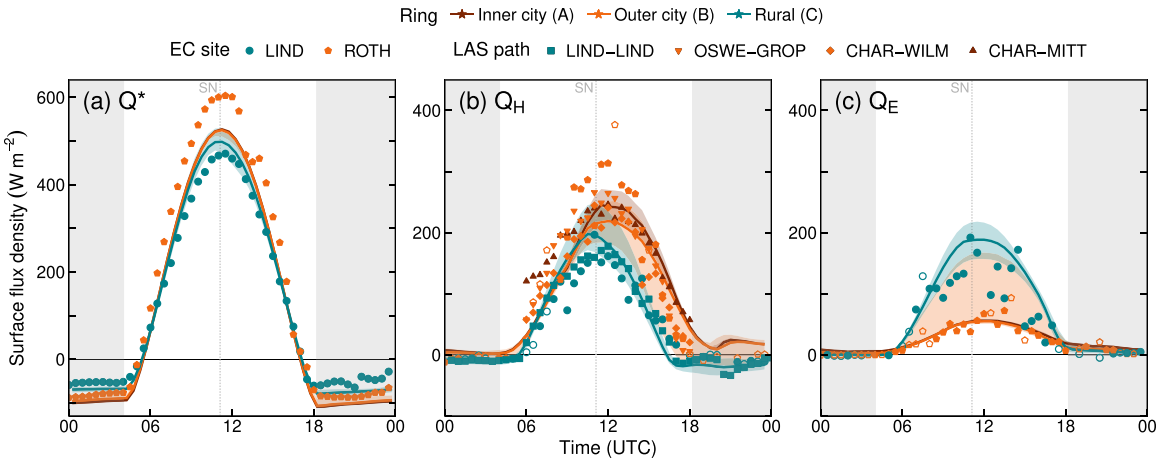

Fig. 4. Modeled (median: lines, interquartile range: shading, 100 m resolution rings A and B, 300 m resolution ring C) and observed fluxes by site/path (symbols; Table 2) on 18 Apr 2022 by ring (color): (a) net all-wave radiation Q^*, (b) turbulent sensible heat Q_H, and (c) turbulent latent heat Q_E. Note that *y* axes differ, all data 30-min averages. EC flux quality flag (Mauder and Foken 2004): 0 = solid and 1 = hollow (appendix C). LAS paths indicated by site codes. Solar noon: SN; sunset to sunrise: gray.

the rural path. There is a stronger urban–rural contrast (+98%) for EC Q_H during the same period and greater EC Q_H at the outer-urban site compared to the inner-city LAS path (Fig. 4b). This is expected as the source areas have different surface characteristics (residential buildings and gardens at ROTH EC compared to the large vegetated park of the CHAR-MITT LAS path; Fig. 3b) and sizes (EC smaller than LAS) (e.g., Ward et al. 2014; Crawford et al. 2017), and therefore, stronger contrasts in surface characteristics may be captured. The larger LAS Q_H during the morning and afternoon in the inner (compared to the outer) city is expected (e.g., Christen and Vogt 2004; Offerle et al. 2006; Ward et al. 2016) given the differences in urban form and function in the sensors' source areas.

Peak Q_H occurs later in the afternoon in the city (compared to the rural) in both the observations and model results (Fig. 4b), consistent with past studies (e.g., Christen and Vogt 2004). The morning rise of modeled Q_H is almost simultaneous for the rings and later than the more variable observations, with inner city earliest and rural latest.

With observed outer-city Q_E only 51% of rural Q_E during midday (Fig. 4c; 1000–1400 UTC), the daytime Bowen ratio Q_H/Q_E is substantially higher (ring B: 4.9 and ring C: 1.0). As the outer city includes pockets of forest and agriculture (Fig. 3b), modeled Q_E interquartile range increases from intergridcell variability.

Given these spatial differences in surface-energy-flux partitioning, we expect boundary layer height (BLH) variability to be observable (Hertwig et al. 2021; Beamesderfer et al. 2023) with 24 ALC and three DWL sensors operating on this day (Fig. 5) using different techniques (appendix B). We classify sites into cohorts (upwind, inner+outer city, downwind, and other rural) using wind direction and rings (Figs. 2 and 3).

From the previous sunset to just before sunrise, a nocturnal low-level jet from northeasterly directions is observed at the top of the nocturnal boundary layer (NBL) by all DWL systems (Fig. 6). The jet maximum first occurs at rural LIND (observed and modeled), given more rapid radiative cooling than in urban areas and negative Q_H (Fig. 4b). This establishes a stable NBL; hence, it is likely that a jet results from an inertial oscillation that forms in response to frictional decoupling from the surface (Blackadar 1957; Oke 1981). Above the rural area, the jet weakens during the night, while it becomes stronger above the city where peak wind speeds are recorded just before sunrise. Turbulent mixing is maintained over the warmer city after sunset, delaying the development of a stable NBL. The jet core is located at a higher altitude at the top of the deeper urban NBL (compared to rural LIND) and upwind outer-city areas (LICH; Fig. 6), as found elsewhere (e.g., Wang et al. 2007; Kallistratova et al. 2009;

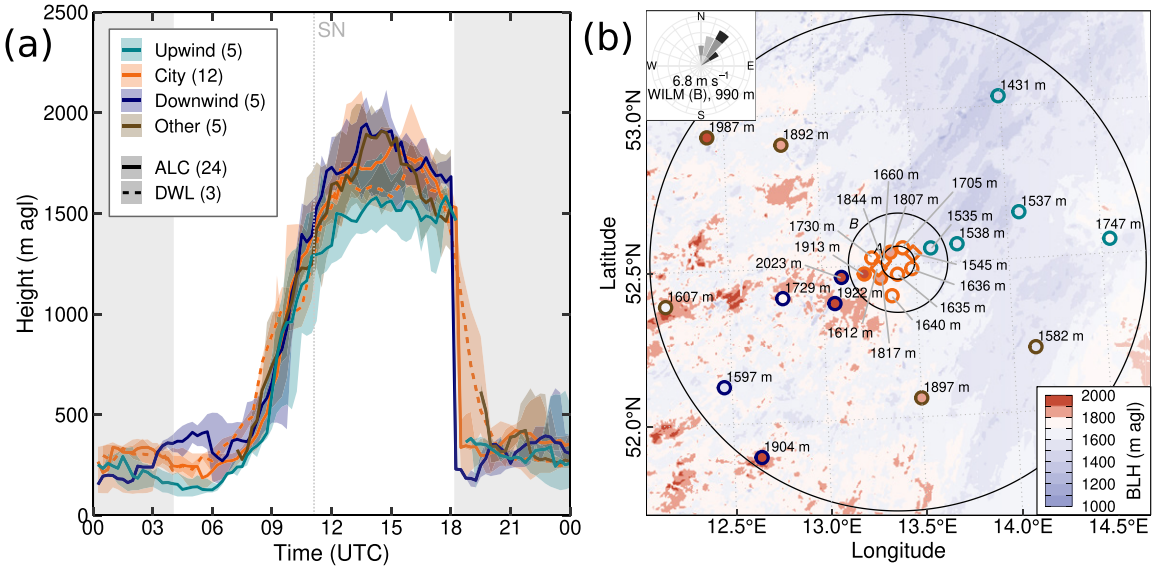

Fig. 5. BLHs on 18 Apr 2022 by group (city: orange; rural: upwind green, downwind blue, lateral/other brown): (a) ALC–MLH (15-min mean), DWL–MH (30-min mean) with median (lines), and range (shading) for number of sites by group/sensor type (Fig. SM1.6 shows the individual time series), and (b) 1300–1500 UTC mean modeled ABL depth (300 m grid; colorbar) and observed MLH and MH (colorbar; labels and symbols: ALC—circle and DWL—diamond) with wind rose 990 m AGL, including mean wind speed during period. Note that observed MLH, MH, and modeled ABL depth are different metrics (e.g., Kotthaus et al. 2018, 2023a). Map projection: ETRS89-extended/LAEA Europe.

Hu et al. 2013; Tsiringakis et al. 2022). While the jet temporal evolution is well modeled (e.g., delayed onset at urban sites), the core is shallower and weaker than observed, especially for urban sites postmidnight, as found by Tsiringakis et al. (2022).

Spatial differences in observed MLH near sunrise (0300–0500 UTC) are evident, with increasing depth at sites along the prevailing wind direction from upwind rural (green, Fig. 5a) (156 m AGL) and city (248 m AGL) to downwind (364 m AGL) (Table SM1.1). In contrast, the modeled NBL is substantially shallower (city: 142 m AGL) (Table SM1.4) but with a small urban plume effect (downwind: 34 m AGL, compare upwind: 13 m AGL and other rural: 13 m AGL).

A new mixed layer replaces the NBL around 0600 UTC, followed by rapid MLH growth around 0800–0830 UTC (Fig. 5a). Although the upwind rural MLH growth starts at a similar time as other areas, the growth rate is slower (248 m h^{-1}; median across sites) than in the city (304 m h^{-1}) and downwind (329 m h^{-1}; Table SM1.1). The model growth rates are spatially consistently ordered for the upwind rural (326 m h^{-1}) and city (391 m h^{-1}; Table SM1.4) sites, unlike the downwind and other rural sites (339 and 379 m h^{-1}).

The MLH continues to grow until about 1300–1500 UTC, with the largest median height downwind (1916 m AGL) and shallowest upwind (1546 m AGL). The city medians are almost

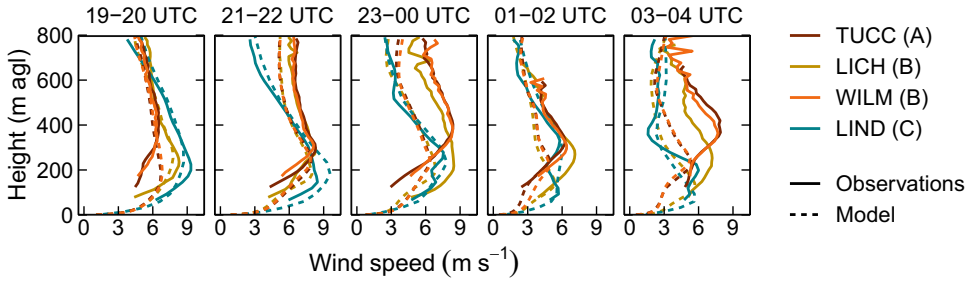

Fig. 6. Hourly mean vertical profiles of wind speed (17–18 Apr 2022) from DWL (solid; 12 scans per hour) and model (dashed; four 15-min instantaneous, gridcell resolution rings A and B: 100 m and ring C: 300 m, 3 × 3 grid cells) by location (color).

identical between the inner-city (1720 m) and outer-city (1729 m) rings. The model cohorts' results have the same spatial pattern as observed but are shallower (Table SM1.4). The modeled afternoon ABL depth northeast of Berlin is shallower than over central and southern areas, consistent with observations in these cohorts (Fig. 5b). Given the sensor and algorithm uncertainties combined in this model comparison, interpretations should be done cautiously (Kotthaus et al. 2018, 2023a). Regional afternoon ALC-derived ABL cloud cover shows little variability with mostly clear-sky conditions. Cloud cover increases from upwind and over city to downwind areas with 0.0, 0.2, and 0.4 okta, suggesting an urban influence (Theeuwes et al. 2019; Vo et al. 2023). With 0.9 okta over the other rural sites (brown circles, Fig. 5b), this is consistent with the BLH regional effect (Fig. 5).

After sunset, the NBL height between 2000 and 2200 UTC is highest above the city (median: 396 m AGL), with the inner city (median: 398 m AGL) deeper than the outer city (360 m AGL). This general behavior is modeled (Table SM1.4), but again shallower than observed.

In comparison with Berlin, urban–rural MLH differences during clear spring days in another large midlatitude city (Paris, France) can be hundreds of meters (Pal et al. 2012) or smaller (Dupont et al. 1999), depending on sites compared and synoptic conditions. Our high-density sensor network combined with high-resolution modeling is critical for detecting regional-scale patterns (Fig. 5b) and the impact of cities on surface–atmosphere coupling. Future analysis of the full *urbisphere*-Berlin dataset will allow comparisons to other long-term studies (e.g., Lotteraner and Piringer 2016; Kotthaus and Grimmond 2018b; Wiegner et al. 2020) but with detailed spatiotemporal information.

In the evening, the canopy-layer near-surface T_{air} is lower on the upwind side of Berlin and higher in ring A and downwind (to SW; Fig. 7a) by 1.5 K comparing downwind to upwind sector (appendix F), with the model reproducing a similar spatial pattern (not shown). This canopy-layer heat advection is expected (Lowry 1977) and often both observed (e.g., Brandsma et al. 2003; Bassett et al. 2016, 2017; Varentsov et al. 2021; Brousse et al. 2022) and modeled (e.g., Bohnenstengel et al. 2011; Heaviside et al. 2015; Varentsov et al. 2018).

An urban plume of nitrogen dioxide (NO_2) extending several 10 km from the city center is observed in satellite data [Fig. 7b; Sentinel-5P Tropospheric Monitoring Instrument (TROPOMI) NO_2; Veefkind et al. 2012]. As NO_2 is released mainly from combustion processes at the surface (Beirle et al. 2011), local emission sources are distinguishable (Fig. 7b).

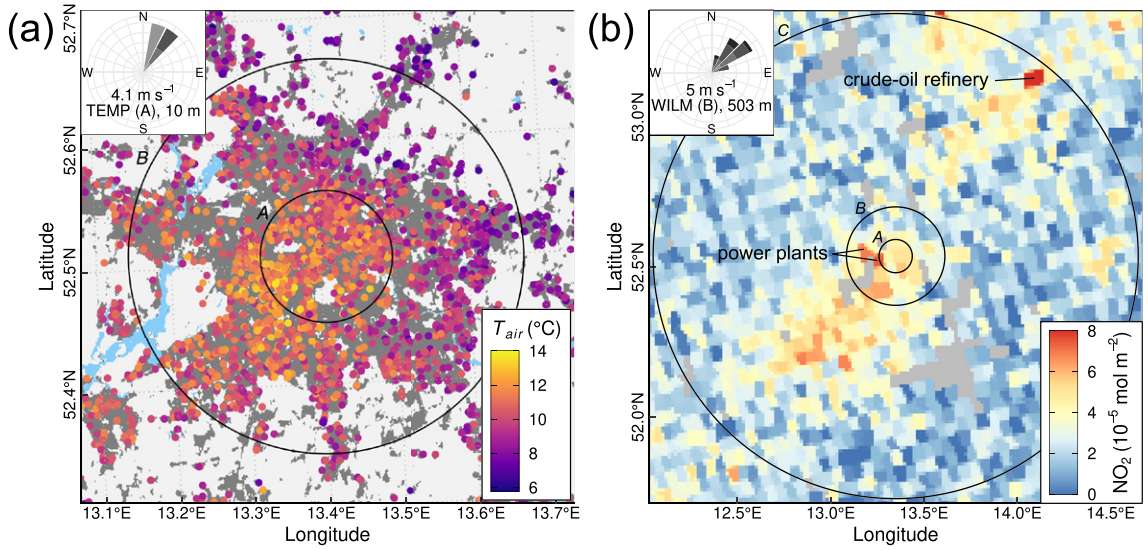

Fig. 7. 18 Apr 2022 (a) mean near-surface air temperature T_{air} for 1900–2200 UTC (data: appendix F) and (b) tropospheric NO_2 column density (source: appendix G) and cloud mask (gray) for 1059 UTC. Wind rose insets for site indicated (height m AGL) and mean wind speed with (a) 10-min data through period and (b) 5-min data for 0800–1100 UTC. Projection: ETRS89-extended/LAEA Europe.

Urban NO_2 hotspots and plumes reported using Earth observations (e.g., Beirle et al. 2011; Lorente et al. 2019; Tack et al. 2019; Finch et al. 2022; Lama et al. 2022; Müller et al. 2022) capture dynamic effects from urban activities, such as COVID-19 lockdown reductions (e.g., Bauwens et al. 2020; Levelt et al. 2022; Schatke et al. 2022). The 1-km satellite-pixel AOD (MODIS MCD19A2 v6; Lyapustin and Wang 2018) indicates regional variability on this day with generally higher values east of Berlin but no discernible urban effect (not shown). However, our ground-based sensors observe significantly ($p < 0.001$; Wilcoxon–Mann–Whitney test) smaller AOD (9%–28% depending on wavelength) at the inner city (FRIE, A) than at the rural site (LIND, C) from 0600 to 0800 UTC, but 18%–87% larger AOD (significant) in the city than in the rural site for 1300–1500 UTC.

Overall, this case shows the benefit of our dense, structured observational network design, when combined with high-resolution NWP modeling, as it allows regional effects along the upwind-city-downwind transect as well as intraurban variability in ABL characteristics to be explored. Multiscale observations and NWP also enable an understanding of surface–atmosphere interactions and urban impacts beyond the built-up area.

b. Case 2: Regional heatwave with deep atmospheric boundary layer. Increasing heatwave frequency, impacting dense populations exposed in cities (Tuholske et al. 2021; Nazarian et al. 2022), requires strategic preparation to support residents and infrastructure (see "Urban form and human-activity cycles" sidebar). For this case, we investigate how Berlin modifies atmospheric conditions during extreme heat, as it remains unclear how the urban ABL responds to heatwaves (e.g., Barlow et al. 2015; Wang and Li 2019).

After two dry months in summer 2022, with little irrigation in Berlin or of regional cropland and forests, most vegetation is stressed. The impact is particularly evident when rural KIEN (pine forest) and MUEN (cherry orchard with semiautomatic irrigation) are compared (Fig. 8). With little soil moisture available, the pine forest has smaller observed Q_E than the cherry orchard, with midday (1000–1400 UTC) Q_E/Q^* of 0.17 at KIEN and Q_E/Q^* of 0.37 at MUEN. Other sites have midday Q_E/Q^* from 0.3 (LIND, C) to 0.23 (ROTH, B) to 0.06 (TUCC, A), with values consistent with EC source-area vegetated fractions of 1.0, 0.45, and 0.24, respectively. Observed outer-city Q_E is higher compared to the spring day as the leaves are now out, resulting in greater leaf area index and irrigation likely in the private properties surrounding the EC site ROTH. The midday storage heat-flux fraction (observed residual; e.g., Christen and Vogt 2004) is inversely related to the vegetation fraction with values of 0.48 (TUCC, A), 0.34 (ROTH, B), 0.30 (MUEN, C), and 0.17 (LIND, C). The midday storage heat-flux fraction at urban ROTH is of similar magnitude as on the spring day, but 50% smaller at rural LIND.

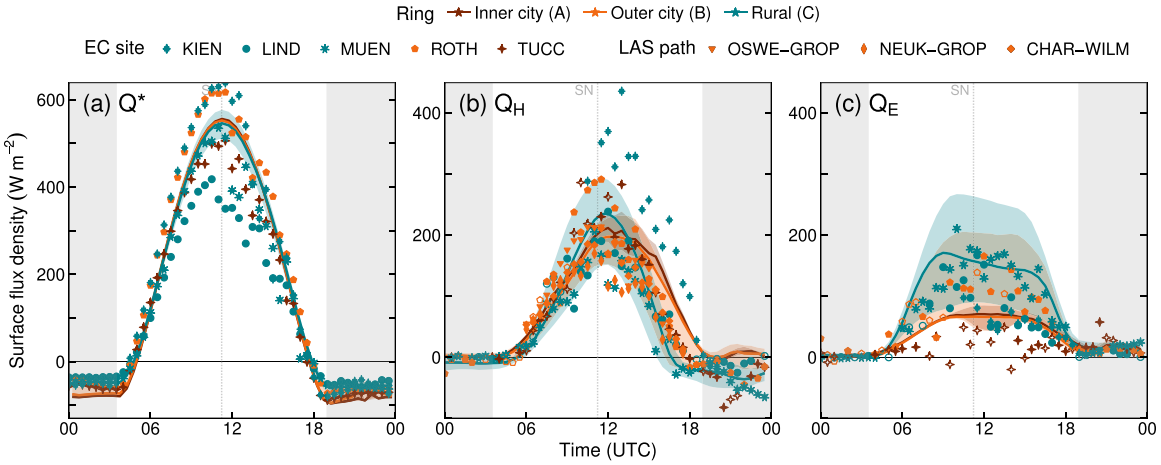

Fig. 8. As in Fig. 4, but for 4 Aug 2022.

The large observed Q_H (compared to Q_E) during midday at all sites results in Bowen ratios >1 for all urban and nonirrigated rural sites (TUCC, A: 6.3; ROTH, B: 1.9; KIEN, C: 5.4; and LIND, C: 2.0), whereas irrigated site MUEN (C) is 0.8. The Q_H/Q^* range is from 0.34 (MUEN, C) to 0.68 (KIEN, C). The modeled rural Q_H is greater than for both urban rings (Fig. 8b), indicating the importance of appropriate initial soil moisture in all areas and model sensitivity to soil-moisture initialization in general.

This large Q_H/Q^* across the region in urban and nonirrigated rural areas results in a deep ABL at the regional scale (Fig. 9). The DWL-derived MH at night is greater than the ALC-derived MLH and has a faster morning growth (Fig. 9a), as found previously when comparing the two BLH types (Kotthaus et al. 2018). About 3 h after sunrise, MLH grows rapidly, with maxima reached between 1500 UTC and sunset (Fig. 9a). Median MLH (1500–1700 UTC) is similar across the region, with 3240 m AGL over the city (rings A + B) and 3265 m AGL over the rural area (ring C). Given the southwesterly wind (Fig. SM1.5), only ANGE is downwind of the city, where the MLH is deeper than over the city but shallower than rural sites upwind or aside the city (Fig. 9a). The evening MH collapses more slowly than the MLH (Fig. 9a), possibly due to waves increasing vertical velocity variance (Lean et al. 2022). Afternoon decay in the modeled BLH varies between sites (Fig. 9b), with the collapse over the city being later than over rural areas and therefore closer to the observed MLH behavior. This is consistent with both our modeled Q_H remaining larger in the city in the evening and longer than observed (Fig. 8b), and previous studies (Simón-Moral et al. 2019; Hertwig et al. 2020).

Consistent with other observation- and model-based heatwave studies (e.g., Zhang et al. 2020), we detect a greater BLH associated with large Q_H (e.g., Wang and Li 2019; Yue et al. 2021; Beamesderfer et al. 2023), low soil moisture (Santanello et al. 2005), and high vapor-pressure deficit (Beamesderfer et al. 2023). The regionally dry conditions make intrasite variability more difficult to assess relative to the short-time-scale variability of processes such as entrainment.

Simultaneous radiosonde launches at an upwind rural (ZOSS; Fig. 3b) and an urban site (GLEI, A; Fig. 3c) indicate a 60-m-deeper ABL over the city (175 m AGL; i.e., 50% increase) than above the rural location (115 m AGL) at 0615 UTC (Fig. 9c and Fig. SM1.8), as found for another summer day (see "Mobile ALC deployment for detecting MLH at high spatial

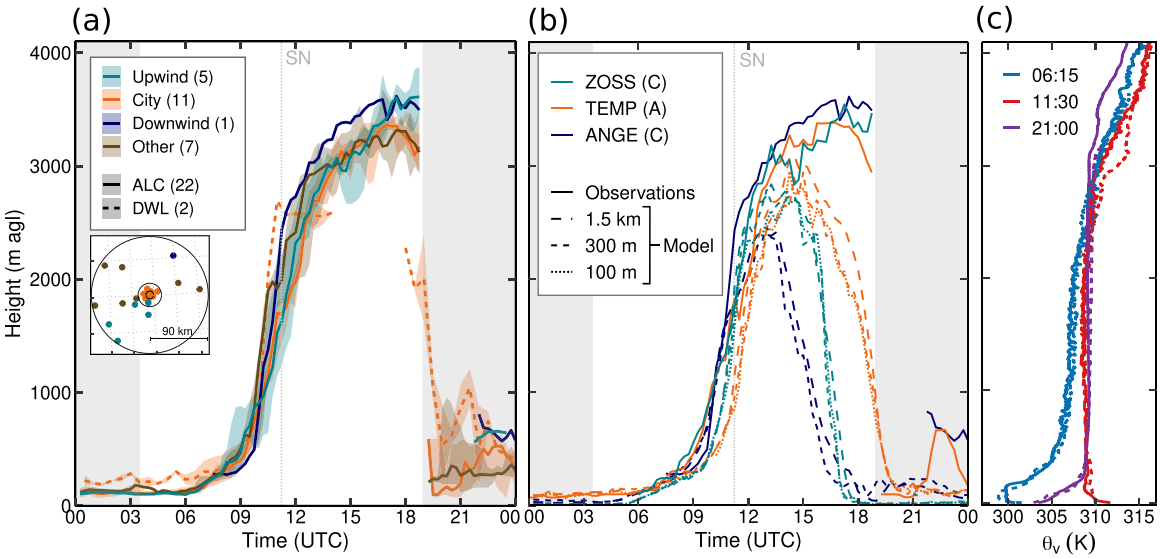

Fig. 9. As in Fig. 5a, but for 4 Aug 2022: (a) ALC–MLH (15-min mean) and DWL–MH (30-min mean) with median (lines) and range (shading) for number of sites by group/sensor type and site map (group color) (Fig. SM1.7 shows the individual time series), (b) observed MLH (solid) and modeled BLH (dashed/dotted; 3 × 3 grid cells) at three sites (rural downwind: ANGE, upwind: ZOSS, and city: TEMP), and (c) radiosonde virtual potential temperature θ_v launched at ZOSS (dashed, C) and GLEI (solid, A) at three times (compare Fig. SM1.8).

resolution" sidebar) and elsewhere during clear-sky summer conditions (e.g., Godowitch et al. 1985, 1987). Consistent with the ALC observations, the daytime radiosonde profiles do not have a systematic urban–rural difference on this day. A weak ABL urban heat island (UHI) of 0.9 K develops in the lowest 80 m below the first rural inversion after the formation of the NBL (2100 UTC; Fig. 9c and Fig. SM1.8).

Near-surface T_{air} is similar between the city center and outskirts during daytime (Fig. 10a), as typical in Berlin's summer (e.g., Fenner et al. 2014, 2017). After sunset, the near-surface UHI (canopy layer; Fig. 10b) is stronger than the BL-UHI, as expected (e.g., Bornstein 1968; Oke and East 1971; Tapper 1990). Both UHI types are induced and modulated by the daytime heat storage of buildings and slower nocturnal cooling rates, leading to higher near-surface T_{air} in the densely built-up inner city (ring A, median T_{air} 30.5°C) compared to the outer city (ring B, median T_{air} 28.7°C) and rural areas (ring C, median T_{air} 27.8°C) (Fig. 10b). Human exposure to such warmer conditions in the city after hot days (Fenner et al. 2019) can be hazardous, especially for the elderly (e.g., Dousset et al. 2010; Gabriel and Endlicher 2011; Laaidi et al. 2012; Scherer et al. 2014; Ho et al. 2017).

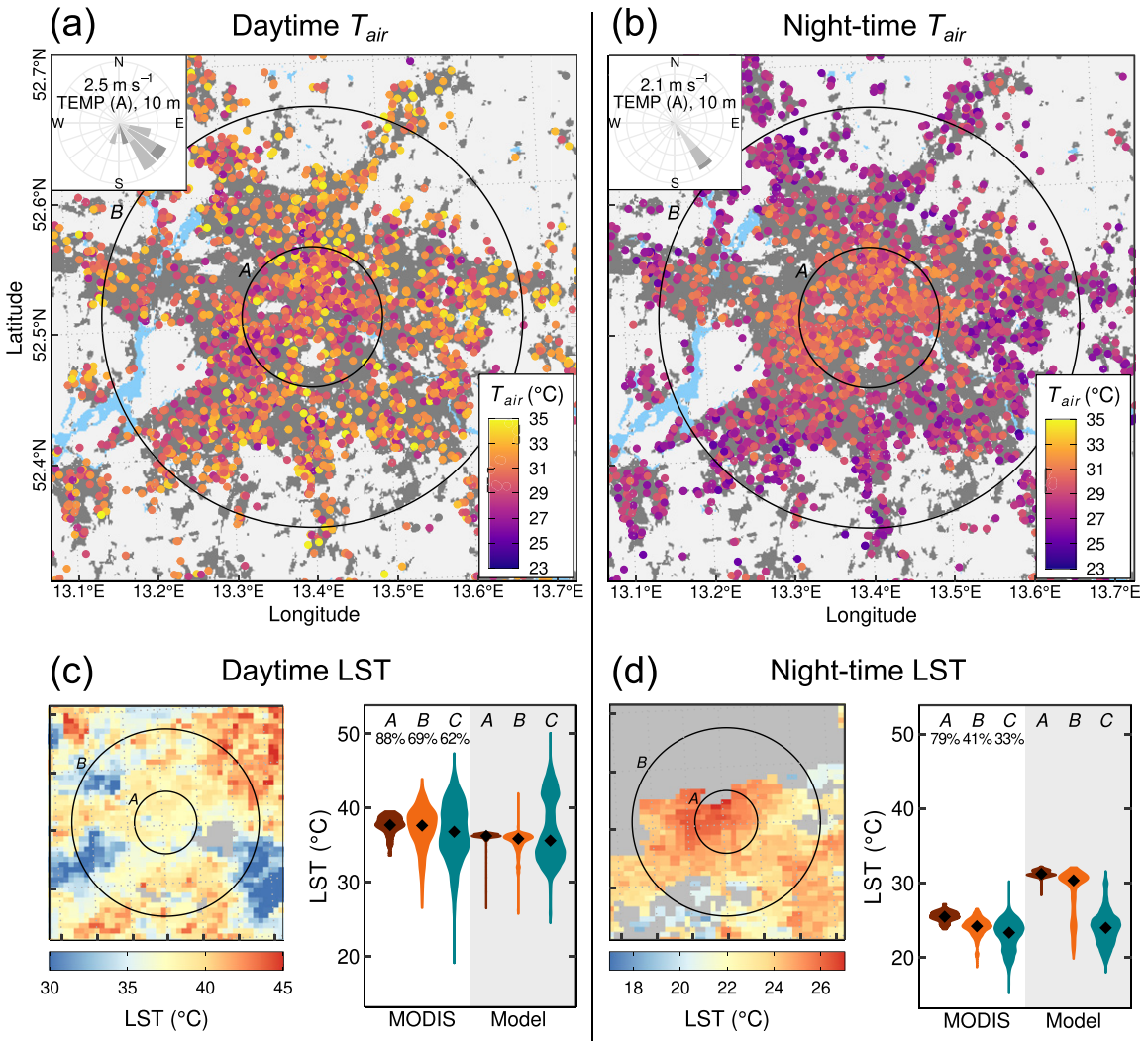

Fig. 10. Mean (a) daytime and (b) nighttime near-surface air temperature T_{air} and (c),(d) LST on 4 Aug 2022. The T_{air} during (a) 0801–1100 UTC and (b) 1901–2200 UTC (data: appendix F). Wind rose insets for site TEMP (10 m AGL) with mean wind speed and 10-min data through periods. LST at (c) 1000 UTC and (d) 2110 UTC (MODIS; appendix G, colorbar scales differ) maps and violin plot distributions (MODIS and model; 300 m grid resolution) for rings A to C with medians (diamond) and data availability after cloud mask (number %; map: gray). Map projections: ETRS89-extended/LAEA Europe.

From the morning LST (Fig. 10c), the general regional land-cover patterns unrelated to the city are evident with relatively cool lakes and forests in the southeast and southwest and relatively warm harvested cropland in the northeast and south. At night, inner-city LST is higher than the outer-city and rural regions (Fig. 10d). Observed and modeled differences in LST between the three rings are more pronounced after sunset than midmorning (Figs. 10c,d). This atypical pattern for temperate cities (e.g., Peng et al. 2012; Bechtel et al. 2019; Sismanidis et al. 2022) is more consistent with arid-climate cities with limited plant-water availability (e.g., Imhoff et al. 2010; Benas et al. 2017; Chakraborty and Lee 2019; Manoli et al. 2020; Sismanidis et al. 2022) because of the regional drought, dry soils, and reduced Q_E (Fig. 8c). Modeled nocturnal surface temperature UHI is larger than observed (Fig. 10d), consistent with the Q_H lag and too large model thermal inertia for built urban surfaces. Note that cloud masking of observed MODIS LST in rings B and C may reduce variability.

In summary, this case highlights ABL characteristics under extreme heatwave conditions, with implications not only for urban areas. Although no systematic urban influence on BLH is detected, the city modulates near-surface conditions which are relevant to human and infrastructure exposure and potentially hazardous. The case demonstrates the benefits from the multitude of remote sensing instruments deployed (appendix B), as well as the challenges and necessity of ensuring all boundary conditions are appropriate for high-resolution NWP (e.g., soil moisture). The wide range of observations deployed allows in-depth evaluation of NWP output to identify where high-resolution models can be improved.

5. Concluding comments

Two case-study days from the yearlong *urbisphere*-Berlin campaign demonstrate the diverse and dynamic nature of city–atmosphere interactions. We conclude with key lessons learnt:

- Concurrent multiscale observations and modeling of surface fluxes and ABL development enhance our understanding of surface–atmosphere interactions. Ground-based and spaceborne observations, when properly aligned with NWP scales and forecast processes, allow us to identify the conditions and processes that NWP systems can model both well and poorly. Such findings are valuable to guide strategic efforts to improve high-resolution urban-scale weather and climate simulations, to address, e.g., the challenge of soil-moisture sensitivity (Hall et al. 2024) during the heatwave day.
- Our systematic transect- and grid-based observational network design permits targeted investigation of urban atmospheric modifications as air travels from rural over city to downwind regions. This provides a clear advantage over traditional urban–rural station pairs or operational networks using infrastructure (e.g., airports), as single rural sites may be influenced by the city in weather situations when they are located downwind (Lowry 1977). With >25 ABL sites, in combination with satellite remote sensing, the timing and intensity of urban effects are dynamically, thermodynamically, and chemically assessable in detail, such as the urban plume detected downwind on the spring day. This extensive dataset is designed with the needs of evaluating high-resolution models at multiple scales.
- Our general characterization of urban form and function with rings to capture predominant urban-density trends helps us to analyze intraurban variability and urban–rural gradients beyond simple urban–rural differences. Combined with the dense sensor network, our approach also allows for more detailed studies on spatial variability at smaller scales within the rings. We demonstrate the benefits of the rings for both network design and observational and modeling data analyses. Designed to be generically applicable, we recommend this approach to be tested in other cities to allow for future intercity comparative studies, while also capturing intracity variability consistently.

- Continuous high-resolution, multiscale yearlong observations embedded in coarser long-term networks are beneficial for analysis and understanding of interactions under both typical and extreme conditions (e.g., heatwaves and air pollution episodes). A year captures different human-activity cycles (e.g., weekend–weekday and seasonal differences), which should be represented dynamically in NWP so they are responsive both regarding impacts on the atmosphere and atmospheric impacts on urban systems (e.g., energy use in the city for heating or cooling; Liu et al. 2022, 2023).
- Design and setup of the campaign network is an iterative process that needs to always keep the overarching goals and complementarity of measurements and processes across scales in view (Fig. 1). This process requires background experience, local partners, flexibility, and time. Here, it took nearly 1 year to plan and set up the whole network, as site scouting, obtaining (or being denied) permissions, and logistics require constant adaptation and replanning. Having complementary sensors to perform under different extremes (e.g., sensor outages and meteorological conditions) is beneficial, as are early data analyses using quick looks and more in-depth studies to identify potential issues.

Future work involving the *urbisphere*-Berlin data will include both detailed analyses of the observations and observation–model comparisons. Examples are year-round ABL dynamics, different methods to diagnose model BLH informed by observations, surface energy fluxes under typical and extreme conditions, or modeled (land) surface temperature compared to multiscale observations.

The transferability of Berlin results to other cities regarding the role of city size (both larger and smaller), the impact of topography (e.g., coastal and elevation range), and/or with different sociocultural backgrounds need to be assessed in future campaigns to fill gaps. *urbisphere*-Paris and *urbisphere*-Bristol campaigns similarly aim at collecting high-resolution city-specific datasets, to enable and support future research, model evaluation, and identify model development needs, focusing on radiation, dispersion, and air pollution meteorology not resolved in the same detail in Berlin. As with *urbisphere*-Berlin, the foci and network designs in these campaigns consider city-specific urban form and function, regional weather and climate, topographic settings, sociotechnological background, and existing long-term observations.

To enhance considerations of differential human exposure, vulnerability, and adaptive capacities in cities, *urbisphere* aims to advance current knowledge of people's behavior and response to weather and climate hazards through dedicated surveys (Iqbal et al. 2024) and agent-based modeling (see "Urban form and human-activity cycles" sidebar; Hertwig et al. 2024), as well as to assess indoor conditions (Xie et al. 2023; Sulzer and Christen 2024), socioeconomic trends and transitions, and feedback between human activities and the atmosphere in urban-scale scenario and forecast models.

urbisphere-Berlin showcases the feasibility and applicability of high-density observations and modeling at multiple scales for multiple purposes that are central to developing IUS (WMO 2019). IUS need to be delivered and assessed across the multiple spatiotemporal scales critical to weather, climate, hydrology, and air quality. These impact, feedback, and support current and future operations across many interacting sectors in cities and their surroundings.

Acknowledgments. We thank all *urbisphere* team members and partners who supported the campaign, including Felix Baab, Josefine Brückmann, Martina Frid, Leonie Grau, Stanley George, Valentina Guacita, Giannis Lantzanakis, Lars Mathes, Emmanouil Panagiotakis, David Parastatidis, Karthik Reddy Buchireddy Sri, Dirk Redepenning, Sebastian Scholz, Ingo Suchland, Timothy Sung, Angela Wendnagel-Beck, and Yuting Wu. We further thank those who provided sites for sensor

installations (including Deutscher Wetterdienst, Technische Universität Berlin, Bezirksamt Charlottenburg-Wilmersdorf, Berlin Senate, Umweltbundesamt, HTW Berlin, and all individuals and external partners), data (including Deutscher Wetterdienst, Rainer Hentschel at Landesbetrieb Forst Brandenburg, Mostafa Sayeed and Sebastian Scholz at BTU, Volker Quaschning and Joseph Bergner at HTW, and the public who share data), and instruments (UKRI NERC AMOF_20220419111152). We thank ICOS for providing the data/facilities at sites KIEN and ROTH and acknowledge AERONET-Europe/ACTRIS for calibration and maintenance services under the European Union's Horizon 2020 research and innovation program (Grant Agreement 654109). We acknowledge the use of Monsoon2, a collaborative facility supplied under the Joint Weather and Climate Research Programme, a strategic partnership between the Met Office and the Natural Environment Research Council. We are thankful to the two reviewers for their constructive and helpful comments. The work is funded by the European Research Council (ERC) under the European Union's Horizon 2020 research and innovation program (Grant Agreement 855005), UKRI EP/V010166/1, and UKRI NE/W002965/1. Some personnel and infrastructure were funded by the Universities of Freiburg, Reading, Stuttgart, and Technische Universität Berlin.

Data availability statement. All data presented are available at https://doi.org/10.5281/zenodo.11235442.

APPENDIX A
Urban Form and Function to Derive Campaign Rings—Data and Processing

The center point and three campaign ring radii (Fig. 2 and Fig. SM1.1) are determined from several processed datasets (Table A1).

APPENDIX B
Ground-Based Remote Sensing—Data Processing

Central to the *urbisphere*-Berlin campaign are the ALC and DWL networks (Fig. 3). We distinguish between methods of determining BLH, following Kotthaus et al. (2018): aerosol-concentration-derived MLH from ALC and turbulence-derived MH from DWL.

Table A1. Data and analysis to create Fig. 2 with 300-m resolution except anthropogenic heat flux which is kept at 500-m resolution.

Characteristic	Data source, spatial resolution	Method
Center point	Marconcini et al. (2021), 10 m	Building fraction ≥ 0.05 at 100-m resolution used to determine the centroid of dissolved vector polygon
Building fraction	Geoportal Berlin (2023), building polygons	Rasterized to 1-m spatial resolution
Vegetated fraction	Zanaga et al. (2022), 10 m	Vegetation = tree + shrub + grass + crop
Building volume *V*	Building polygons: Geoportal Berlin (2023), GeoBasis-DE/LGB (2023a) Building heights: Geoportal Berlin (2021, 2022b), GeoBasis-DE/LGB (2022, 2023b)	Mean building height derived from digital surface and digital elevation models at building footprint scale Building scale: V_{BS} = height*area Grid scale: total V_{BS}/grid plan area (300 m resolution)
Residential population density	Population: Geoportal Berlin (2022a), StatBB (2021) Administrative boundary block (Berlin) or municipalities (Brandenburg): GeoBasis-DE/BKG (2021)	Administrative-scale data downscaled to V_{BS} constrained by administrative (residential + mixed-use) *V*, aggregated to 300-m grid
Anthropogenic heat flux	Varquez et al. (2021), 500 m	

The three **ALC** types deployed allow vertical profiles of attenuated backscatter, cloud-base height, cloud-cover fraction, and aerosol-concentration-based MLH to be obtained. The Vaisala CL61 additionally allows the aerosol shape to be inferred from the linear depolarization ratio. The saved raw profile measurements every 15 s (similar to, e.g., Kotthaus and Grimmond 2018a) for all device types ensure independent measurements across the entire vertical measurement range of up to 15.4 km and consistency across devices, with range gates of 4.8 m (CL61), 10 m (Vaisala CL31), and 15 m (Lufft/OTT HydroMet CHM15k). The ALC data processing to obtain MLH from the raw data includes the following:

1) Data conversion
   - Raw instrument data converted to Network Common Data Form (netCDF) format using raw2l1 (Drouin et al. 2022) to create one file per day with coordinated universal time (UTC)
2) Instrument-specific processing and calibration

   CHM15k:
   - Optical overlap correction (Hervo et al. 2016), using Overlap_corr (Van Hove et al. 2023a)
   - Rayleigh calibration (Wiegner and Geiß 2012) using median calibration value during 1 October 2021–30 September 2022, removing outliers (lidar constant > 10^{12})

   CL31:
   - Background and near-range signal correction using termination hood measurements of 1-h length (Kotthaus et al. 2016)
3) Automatic MLH detection

   CL61 and CHM15k:
   - STRATfinder (Kotthaus et al. 2020, 2023b) MLH detection with Kotthaus et al. (2020) settings with output at 30-m vertical resolution and 60-s block averages
   - Automatic quality control (QC) using QC STRATfinder (Van Hove et al. 2023b), followed by manual QC: comparing detected MLH and attenuated backscatter profiles

   CL31:
   - Characterising the Atmospheric Boundary Layer Based on ALC Measurements (CABAM) (Kotthaus et al. 2018) MLH detection: using 15-min running averages

Incomplete optical overlap prevents the Lufft CHM15k from providing MLH below 200–250 m AGL (e.g., Kotthaus et al. 2020; Wiegner et al. 2020), hindering, e.g., shallow NBL detection (Figs. 5a, 9a). While Vaisala CL31 and CL61 can provide robust estimates for shallow layers (~50–70 m AGL) after correcting for near-range artifacts (Kotthaus et al. 2016; Kotthaus and Grimmond 2018a), the CL31's lower laser power and signal-to-noise ratio limit utility after the growth phase (0900–1000 UTC; Fig. 9a) until sunset. The CL61 observes the peak MLH. Sometimes device-specific differences can hamper MLH comparisons (Kotthaus et al. 2023a), but the MLH estimates are consistent across ALC types derived from the two automatic algorithms.

The five DWL (HALO Photonics/Lumibird StreamLine and StreamLine XR) provide vertical profiles of attenuated backscatter, vertical and horizontal wind components, and turbulence-derived MH. Devices installed on building roofs (4) and the ground (LICH and LIND) (Table 2) in the urban area had 200 nonoverlapping gates of 18-m length (maximum range = 3600 m AGL). The LIND device operated with 100 nonoverlapping gates of 30-m length (maximum range = 3000 m AGL) and a focus of 500 m. For other settings and scan strategies, see supplemental material 2.

DWL data processing uses the "HALO lidar toolbox" (Manninen et al. 2023) as follows:

- Calibrate raw data by correcting for background artifacts (Manninen et al. 2016) and ripple removal if background files are available (Vakkari et al. 2019)

- Retrieve horizontal wind components from 12-point velocity–azimuth display (VAD) scans at 75° elevation angle (Päschke et al. 2015; Newsom et al. 2017)
- Calculate 30-min vertical velocity statistics (mean, standard deviation, variance, skewness, and kurtosis) from vertical stare scan (90° elevation)

Data with signal-to-noise ratio (SNR + 1) <1.005 are excluded from further analysis. Hourly mean wind profiles are calculated from the 12 VAD scans per hour. MH is derived as the height where the vertical velocity variance < 0.1 m^2 s^{-2} (Barlow et al. 2011, 2015; Kotthaus et al. 2018).

With the applied DWL setup and scan strategy, the devices failed to detect the top of the ABL during midday and afternoon periods on days with a deep ABL (including the case-study days), hindering MH detection. Further instrument-specific issues relate to some DWL devices overheating and switching off during hot conditions (e.g., devices at LICH and TUCC during case 2).

APPENDIX C
Turbulent Fluxes—Data Processing

Turbulent sensible heat fluxes Q_H are obtained from both large-aperture scintillometer (LAS) and eddy covariance (EC) measurements. The EC systems also provide other turbulent fluxes, such as latent heat Q_E and carbon dioxide F_{CO2}.

The three LAS models (Scintec BLS450, BLS900, and BLS2000) transmitter–receiver pairs, installed on tall building roofs (Fig. 3c), have different pathlengths (2549 to 6380 m; Table C1). The LIND rural path (Fig. 3b and Table 2) above cropland/grassland is 4.8-km long.

The LAS observed beam intensity variance is used to derive Q_H. At LIND, calculations follow Van Kesteren et al. (2015) with error compensations during low crosswind episodes (high-pass filter) and accounting for signal saturation. Manufacturer's saturation and extinction correction and Thiermann and Grassl (1992) similarity functions are used in calculating Q_H.

For the urban paths, the LAS refractive index structure parameter C_n^2 ($m^{-2/3}$) is used with the GROP (Table 2) air temperature T_{air} and relative humidity (RH), and WILM gate 5 (~173 m AGL; Table 2), DWL-derived horizontal wind speed data. The LAS source area is calculated using a modification to Kormann and Meixner (2001) and a digital elevation model (Geoportal Berlin 2023; rasterized to 2 m × 2 m) to obtain the weighted roughness length, displacement height, LAS effective beam height (Table C1), and wind speed at the LAS effective beam height. Meteorological variables and morphometric parameters are used to iteratively solve for vertical scaling variables of wind (i.e., friction velocity u^*) and temperature scaling variable T^* and Q_H (Crawford et al. 2017; Saunders et al. 2024). Here, stable conditions are excluded based on visual inspection of C_n^2 and Q_H.

The different models of EC sensors involve both sonic anemometer thermometers (Gill Instruments R3-50 and WindMaster Pro, and Metek USA-1) and infrared gas analyzers

Table C1. LAS path and site details (Table 2). SA-G: Scintec AG, Germany.

Path	Model; manufacturer	Pathlength (m)	Effective beam height (m AGL)
CHAR-MITT	BLS2000; SA-G	6380	71.3
CHAR-WILM	BLS450; SA-G	2833	57.4
LIND-LIND	BLS900; SA-G	4800	43.0
NEUK-GROP	BLS450; SA-G	2549	26.3
	BL900; SA-G		
OSWE-GROP	BLS2000; SA-G	4993	42.8

(Campbell Scientific IRGASON, LI-COR LI7500) (Table 2). Timing and details of gas analyzer calibrations for water vapor (H_2O) and carbon dioxide (CO_2) differ by site:

- KIEN: CO_2 (zero, one span) and H_2O (zero, one span), in-field calibration: March 2021, March 2022, and September 2023
- LIND: H_2O (9 points), laboratory calibration of two sensors: March 2020 and January 2022
- MITT: CO_2 (zero, one span) and H_2O (zero), laboratory calibration: November 2021
- MUEN: CO_2 (zero, one span) and H_2O (zero), in-field calibration: August 2022
- ROTH: CO_2 (zero, one span) and H_2O (zero), in-field calibration: July 2021, March 2022, and October 2022
- TUCC: CO_2 (zero, one span) and H_2O (zero), in-field calibration: July 2021, March 2022, and October 2022

CO_2 calibration involved one zero (Zero Air Generator 31022, Campbell Scientific) and one span gas (CO_2 concentration 450 or 500 ppm). H_2O calibration involved zero gas (Zero Air Generator 31022, Campbell Scientific; MITT, MUEN, ROTH, and TUCC), at KIEN nitrogen gas for zero offset (≥99.999 mol %), a dewpoint generator (LI-610, LI-COR, dewpoint 10°C) and one span gas (CO_2 concentration 400 ppm), and at LIND a dewpoint generator (LI-610, LI-COR) and a chilled-mirror hygrometer (Dew Prime II, Edgetech) to measure dewpoint between 1° and 21°C in 5 K steps.

Data processing to obtain 30-min fluxes involves the following:

1) Using slightly different versions of the EddyPro (LI-COR 2022) software with double coordinate rotation (except KIEN) such as follows:
   - ROTH and TUCC: version 6.2, with other details as in Vulova et al. (2021)
   - LIND and MITT: analogously to ROTH and TUCC
   - MUEN: v7.0.9
   - KIEN: v7.0.9 but with sector-wise planar fit with six sectors
2) Automatic QC to exclude data are as follows:
   - During maintenance times
   - With EddyPro quality flag 2 (0-1-2 system; Mauder and Foken 2004: 0 = high-quality data, use in fundamental research possible; 1 = moderate quality data, no restrictions for use in long term observation programs; and 2 = low data quality, gap filling necessary)
   - During times with flow distortion from sensor mounting. For MITT, only data for wind direction 220°–360°, 0°–35° are retained due to building orientation
3) Flux footprint calculations
   - Use the Kljun et al. (2015, 2023) model with MLH from the ALC observations at TUCC and FICH (for EC data at ROTH)
4) Bowen ratio calculated as Q_H/Q_E

CO_2 fluxes (Fig. SB1) are daily, daytime, and nighttime mean workdays and nonworkdays (e.g., weekend and public holidays).

APPENDIX D
Radiation Fluxes and Aerosol Optical Depth—Data Processing

The radiation, aerosol optical depth (AOD), and AWS sensors are sampled at ≥0.1 Hz. All radiometers on sun trackers and sun photometers are regularly cleaned and relevelled (if necessary) at 2–3-weekly intervals. QC processing involves removing maintenance periods.

All *urbisphere* radiation fluxes are 6-s measurements, with datalogger calculated 1-min mean. Radiation fluxes at ROTH and TUCC are measured at 5-s intervals, at LIND and MUEN

at 1-s intervals, and at KIEN at 20-s intervals, all averaged to 1-min means. Here, 30-min means are used. Net all-wave radiation Q^* is calculated from the shortwave (K) and longwave (L), downwelling (↓), upwelling (↑) fluxes: $Q^* = (K\downarrow - K\uparrow) + (L\downarrow - L\uparrow)$, and the albedo α from $\alpha = K\uparrow/K\downarrow$

All three AOD sensor (CIMEL CE318-T) data are automatically uploaded and processed (AERONET 2023). The 5-min AOD data are quality controlled to AERONET Level 2.0 AOD (AERONET 2007).

APPENDIX E
Radiosonde—Data Processing

The Windsond S1H3-S/R Sparv Embedded AB radiosondes (Sparv 2019) provide T_{air}, RH, air pressure, altitude, and geographic location, as well as derived wind speed and heading (wind direction). Latex balloons, inflated with helium to a circumference of ~1.23 m, had a sonde suspended ~5 m below, during their ~2 m s^{-1} ascent. The Windsond software (v2.112) captured the raw data.

QC of sonde data included prelaunch comparison of sonde data to nearby stations:

1) Pressure: Sonde air pressure (adjusted to 0 m AGL) is corrected using the barometric formula (Klose 2016) after comparison with the nearest DWD air pressure observations (DWD 2023b). With a sonde accuracy of 1 hPa (Sparv 2019), only sondes with absolute altitude-corrected pressure differences >1 hPa are corrected using the determined offset (Table E1, mostly negative) to adjust the sonde's pressure profile.
2) Air temperature T_{air}: The closest 2-m T_{air} site with similar local-scale characteristics to GLEI (grassed park) is TEMP, with an altitude difference of 10 m. The T_{air} was compared using altitude-corrected values (environmental lapse rate of −6.5 K km^{-1}; DWD 2023b). However, given the 3.4-km spatial separation between the sites and since inner-city T_{air} variability might be considerable (TEMP vs GLEI), no adjustments are made despite T_{air} differences existing (Table E1). At ZOSS and RAGO comparison, T_{air} is measured at 2.2 m AGL (see "Mobile ALC deployment for detecting MLH at high spatial resolution" sidebar). No corrections are made to the sonde data to avoid introducing inconsistencies, given the lack of comparative data at GLEI. Calculated differences between radiosondes and station data (Table E1) vary between −0.91 and 2.43 K.
3) RH: Analogous to T_{air}, no corrections are made (Table E1).

Virtual potential temperature θ_v is calculated from T_{air}, RH, and corrected air pressure with the "aiRthermo" package (Saénz et al. 2018). Inversion heights are determined using the parcel method (lowest height above ground when θ_v is $\geq\theta_v$ at 0 m AGL before each ascent; Holzworth 1964; Seibert et al. 2000).

APPENDIX F
Crowd Weather Stations—Data Processing

Publicly available Berlin and surrounding regions' (Netatmo 2023) 1-h mean air-temperature data from privately owned weather stations are accessed via an application programming interface (API) and processed (Fenner et al. 2021):

- QC using CrowdQC+ (Fenner et al. 2021) with level "o1" selected
- All height adjusted to 45 m MSL assuming an environmental lapse rate of −6.5 K km^{-1}
- Means calculated if ≥2 valid values available for a site in time periods analyzed (Figs. 7 and 10)

Table E1. Radiosonde prelaunch differences in measurement variables compared to nearby observations.

Launch time (UTC)	Launch site	Comparison site (DWD ID)	Δ Air pressure (hPa)	Δ Air temperature (K)	Δ Relative humidity (%)
4 Aug 2022 0615	GLEI	TEMP (433)	−6.42	1.10	−3.15
4 Aug 2022 0615	ZOSS	Berlin Brandenburg (427)	−6.24		
		ZOSS		2.43	−4.19
4 Aug 2022 1130	GLEI	TEMP (433)	−6.87	1.75	2.75
4 Aug 2022 1130	ZOSS	Berlin Brandenburg (427)	−6.18		
		ZOSS		0.74	−0.24
4 Aug 2022 2100	GLEI	TEMP (433)	−7.11	−0.91	3.25
4 Aug 2022 2100	ZOSS	Berlin Brandenburg (427)	0.28		
		ZOSS		−0.51	−0.98
11 Aug 2022 0615	GLEI	TEMP (433)	−6.75	0.28	0.05
11 Aug 2022 0615	RAGO	Berlin Brandenburg (427)	−5.38		
		RAGO		1.66	−6.04

Advection effect (18 April 2022) estimated as follows :

1) Group all stations into sectors northeast (NE), southeast (SE), SW, and northwest (NW), using city center point. With northeasterly wind direction (Fig. 7a), NE = upwind and SW = downwind.
2) Calculate mean air temperature per local climate zone (LCZ), ≥5 sites per LCZ.
3) Select LCZ present in both sectors (upwind and downwind): 2, 4, 5, 6, 8, 9, 12, and 13.
4) Calculate mean air-temperature difference per LCZ (downwind–upwind) and then average across LCZ.

APPENDIX G
Satellite Data—Data Processing

Summer IOP satellite data include Sentinel-3 (sea and land surface temperature radiometer, nitrogen dioxide column density), Moderate Resolution Imaging Spectroradiometer (MODIS), Advanced Spaceborne Thermal Emission and Reflection Radiometer (ASTER), Ecosystem Spaceborne Thermal Radiometer Experiment on Space Station (ECOSTRESS, and Landsat overpasses. Used data are as follows:

18 April 2022

- 1059 UTC: Sentinel-5P TROPOMI tropospheric nitrogen dioxide column density product (Copernicus 2022; Veefkind et al. 2012) accessed from Google Earth Engine (Gorelick et al. 2017)
- 0940, 1115, and 1135 UTC (*Aqua* and *Terra*) MODIS AOD product MCD19A2 v6 (Lyapustin and Wang 2018)

4 August 2022

- 1000 and 2110 UTC MODIS LST data (Wan et al. 2021, including atmosphere and emissivity correction). Further data processing includes using only
- Cloud-free pixels (cloud flag "00" bits 5 and 4)
- Pixels with QC flag 00 (bits 1 and 0), "pixel produced, good quality, not necessary to examine more detailed QA" (Wan 2019)

APPENDIX H
SIDEBAR 1 Data Analysis

Data for the sidebar "Urban form and human-activity cycles" are as follows:

- CO_2 fluxes (appendix C)
- residential population density and building volumes (Table A1)
- NR to R building volume ratios calculated at 300-m grid resolution with aggregated building volumes by type after splitting "mixed-use" buildings equally between NR and R
- Remainder is given in Table H1

Table H1. Data sources and analysis for the sidebar "Urban form and human-activity cycles".

Characteristic	Resolution	Data source	Processing notes
Building function	Building scale	Geoportal Berlin (2023)	Detailed building function attributes grouped into broader categories of R, NR, and mixed use
Building form typology (residential)	Building scale	Geoportal Berlin (2023)	Existing residential building form attributes used and extrapolated in case of missing classifications by considering the characteristics (e.g., footprint area statistics and number and type of neighboring buildings) of known types
Land use	Vector	Geoportal Berlin (2023)	Selected categories displayed as is
Public road space	Vector	Geoportal Berlin (2014)	Selected categories displayed as is
Energy use—district heating	Berlin block boundaries	Geoportal Berlin (2022c)	Qualitative indicator of use or not

References

AERONET, 2007: AERONET data processing. Accessed 12 December 2023, https://aeronet.gsfc.nasa.gov/new_web/system_descriptions_processing.html.

——, 2023: AERONET Aerosol Robotic Network. Accessed 12 December 2023, https://aeronet.gsfc.nasa.gov/.

Allwine, J., and M. Leach, 2007: Editorial. *J. Appl. Meteor. Climatol.*, **46**, 2017–2018, https://doi.org/10.1175/JAM9044.1.

Allwine, K. J., J. H. Shinn, G. E. Streit, K. L. Clawson, and M. Brown, 2002: Overview of URBAN 2000: A multiscale field study of dispersion through an urban environment. *Bull. Amer. Meteor. Soc.*, **83**, 521–536, https://doi.org/10.1175/1520-0477(2002)083<0521:OOUAMF>2.3.CO;2.

Baklanov, A., and Coauthors, 2018: From urban meteorology, climate and environment research to integrated city services. *Urban Climate*, **23**, 330–341, https://doi.org/10.1016/j.uclim.2017.05.004.

Ban, N., and Coauthors, 2021: The first multi-model ensemble of regional climate simulations at kilometer-scale resolution, Part I: Evaluation of precipitation. *Climate Dyn.*, **57**, 275–302, https://doi.org/10.1007/s00382-021-05708-w.

Barlow, J., and Coauthors, 2017: Developing a research strategy to better understand, observe and simulate urban atmospheric processes at kilometer to sub-kilometer scales. *Bull. Amer. Meteor. Soc.*, **98**, ES261–ES264, https://doi.org/10.1175/BAMS-D-17-0106.1.

Barlow, J. F., 2014: Progress in observing and modelling the urban boundary layer. *Urban Climate*, **10**, 216–240, https://doi.org/10.1016/j.uclim.2014.03.011.

——, T. M. Dunbar, E. G. Nemitz, C. R. Wood, M. W. Gallagher, F. Davies, E. O'Connor, and R. M. Harrison, 2011: Boundary layer dynamics over London, UK, as observed using Doppler lidar during REPARTEE-II. *Atmos. Chem. Phys.*, **11**, 2111–2125, https://doi.org/10.5194/acp-11-2111-2011.

——, C. H. Halios, S. E. Lane, and C. R. Wood, 2015: Observations of urban boundary layer structure during a strong urban heat island event. *Environ. Fluid Mech.*, **15**, 373–398, https://doi.org/10.1007/s10652-014-9335-6.

Bassett, R., X. Cai, L. Chapman, C. Heaviside, J. E. Thornes, C. L. Muller, D. T. Young, and E. L. Warren, 2016: Observations of urban heat island advection from a high-density monitoring network. *Quart. J. Roy. Meteor. Soc.*, **142**, 2434–2441, https://doi.org/10.1002/qj.2836.

——, ——, ——, ——, and ——, 2017: The effects of heat advection on UK weather and climate observations in the vicinity of small urbanized areas. *Bound.-Layer Meteor.*, **165**, 181–196, https://doi.org/10.1007/s10546-017-0263-0.

Bauwens, M., and Coauthors, 2020: Impact of coronavirus outbreak on NO_2 pollution assessed using TROPOMI and OMI observations. *Geophys. Res. Lett.*, **47**, e2020GL087978, https://doi.org/10.1029/2020GL087978.

Beamesderfer, E. R., and Coauthors, 2023: The role of surface energy fluxes in determining mixing layer heights. *Agric. For. Meteor.*, **342**, 109687, https://doi.org/10.1016/j.agrformet.2023.109687.

Bechtel, B., M. Demuzere, G. Mills, W. Zhan, P. Sismanidis, C. Small, and J. Voogt, 2019: SUHI analysis using Local Climate Zones – A comparison of 50 cities. *Urban Climate*, **28**, 100451, https://doi.org/10.1016/j.uclim.2019.01.005.

Becker, A., B. Scherer, M. Memmesheimer, and H. Geiß, 2002: Studying the city plume of Berlin on 20 July 1998 with three different modelling approaches. *J. Atmos. Chem.*, **42**, 41–70, https://doi.org/10.1023/A:1015776331339.

Beirle, S., K. F. Boersma, U. Platt, M. G. Lawrence, and T. Wagner, 2011: Megacity emissions and lifetimes of nitrogen oxides probed from space. *Science*, **333**, 1737–1739, https://doi.org/10.1126/science.1207824.

Benas, N., N. Chrysoulakis, and C. Cartalis, 2017: Trends of urban surface temperature and heat island characteristics in the Mediterranean. *Theor. Appl. Climatol.*, **130**, 807–816, https://doi.org/10.1007/s00704-016-1905-8.

Best, M. J., and Coauthors, 2011: The Joint UK Land Environment Simulator (JULES), model description – Part 1: Energy and water fluxes. *Geosci. Model Dev.*, **4**, 677–699, https://doi.org/10.5194/gmd-4-677-2011.

Birkmann, J., T. Welle, W. Solecki, S. Lwasa, and M. Garschagen, 2016: Boost resilience of small and mid-sized cities. *Nature*, **537**, 605–608, https://doi.org/10.1038/537605a.

Blackadar, A. K., 1957: Boundary layer wind maxima and their significance for the growth of nocturnal inversions. *Bull. Amer. Meteor. Soc.*, **38**, 283–290, https://doi.org/10.1175/1520-0477-38.5.283.

Bohnenstengel, S. I., S. Evans, P. A. Clark, and S. Belcher, 2011: Simulations of the London urban heat island. *Quart. J. Roy. Meteor. Soc.*, **137**, 1625–1640, https://doi.org/10.1002/qj.855.

——, and Coauthors, 2015: Meteorology, air quality, and health in London: The ClearfLo project. *Bull. Amer. Meteor. Soc.*, **96**, 779–804, https://doi.org/10.1175/BAMS-D-12-00245.1.

Bonn, B., and Coauthors, 2016: BAERLIN2014 – The influence of land surface types on and the horizontal heterogeneity of air pollutant levels in Berlin. *Atmos. Chem. Phys.*, **16**, 7785–7811, https://doi.org/10.5194/acp-16-7785-2016.

Bornstein, R. D., 1968: Observations of the urban heat island effect in New York City. *J. Appl. Meteor.*, **7**, 575–582, https://doi.org/10.1175/1520-0450(1968)007<0575:OOTUHI>2.0.CO;2.

Boutle, I. A., J. E. J. Eyre, and A. P. Lock, 2014: Seamless stratocumulus simulation across the turbulent gray zone. *Mon. Wea. Rev.*, **142**, 1655–1668, https://doi.org/10.1175/MWR-D-13-00229.1.

Brandsma, T., G. P. Können, and H. R. A. Wessels, 2003: Empirical estimation of the effect of urban heat advection on the temperature series of De Bilt (The Netherlands). *Int. J. Climatol.*, **23**, 829–845, https://doi.org/10.1002/joc.902.

Brousse, O., C. Simpson, N. Walker, D. Fenner, F. Meier, J. Taylor, and C. Heaviside, 2022: Evidence of horizontal urban heat advection in London using six years of data from a citizen weather station network. *Environ. Res. Lett.*, **17**, 044041, https://doi.org/10.1088/1748-9326/ac5c0f.

Buchhorn, M., B. Smets, L. Bertels, B. De Roo, M. Lesiv, N.-E. Tsendbazar, M. Herold, and S. Fritz, 2020: Copernicus Global Land Service: Land Cover 100m: Collection 3: Epoch 2019: Globe. Zenodo, accessed 14 December 2023, https://doi.org/10.5281/zenodo.3939049.

Bush, M., and Coauthors, 2023: The second Met Office Unified Model–JULES Regional Atmosphere and Land configuration, RAL2. *Geosci. Model Dev.*, **16**, 1713–1734, https://doi.org/10.5194/gmd-16-1713-2023.

Capel-Timms, I., S. T. Smith, T. Sun, and S. Grimmond, 2020: Dynamic Anthropogenic activitieS impacting Heat emissions (DASH v1.0): Development and evaluation. *Geosci. Model Dev.*, **13**, 4891–4924, https://doi.org/10.5194/gmd-13-4891-2020.

Chakraborty, T., and X. Lee, 2019: A simplified urban-extent algorithm to characterize surface urban heat islands on a global scale and examine vegetation control on their spatiotemporal variability. *Int. J. Appl. Earth Obs. Geoinf.*, **74**, 269–280, https://doi.org/10.1016/j.jag.2018.09.015.

Changnon, S. A., F. A. Huff, and R. G. Semonin, 1971: METROMEX: An investigation of inadvertent weather modification. *Bull. Amer. Meteor. Soc.*, **52**, 958–968, https://doi.org/10.1175/1520-0477(1971)052<0958:MAIOIW>2.0.CO;2.

Ching, J., and Coauthors, 2018: WUDAPT: An urban weather, climate and environmental modeling infrastructure for the Anthropocene. *Bull. Amer. Meteor. Soc.*, **99**, 1907–1924, https://doi.org/10.1175/BAMS-D-16-0236.1.

Christen, A., and R. Vogt, 2004: Energy and radiation balance of a central European city. *Int. J. Climatol.*, **24**, 1395–1421, https://doi.org/10.1002/joc.1074.

Chrysoulakis, N., and Coauthors, 2023: Copernicus for urban resilience in Europe. *Sci. Rep.*, **13**, 16251, https://doi.org/10.1038/s41598-023-43371-9.

Clark, D. B., and Coauthors, 2011: The Joint UK Land Environment Simulator (JULES), model description – Part 2: Carbon fluxes and vegetation dynamics. *Geosci. Model Dev.*, **4**, 701–722, https://doi.org/10.5194/gmd-4-701-2011.

Copernicus, 2022: Copernicus Sentinel data 2022, "tropospheric_NO2_column_number_density". Google Earth Engine, accessed 13 December 2023, https://developers.google.com/earth-engine/datasets/catalog/COPERNICUS_S5P_OFFL_L3_NO2#description.

Crawford, B., C. S. B. Grimmond, H. C. Ward, W. Morrison, and S. Kotthaus, 2017: Spatial and temporal patterns of surface-atmosphere energy exchange in a

dense urban environment using scintillometry. *Quart. J. Roy. Meteor. Soc.*, **143**, 817–833, https://doi.org/10.1002/qj.2967.

Davies, T., M. J. P. Cullen, A. J. Malcolm, M. H. Mawson, A. Staniforth, A. A. White, and N. Wood, 2005: A new dynamical core for the Met Office's global and regional modelling of the atmosphere. *Quart. J. Roy. Meteor. Soc.*, **131**, 1759–1782, https://doi.org/10.1256/qj.04.101.

Dousset, B., F. Gourmelon, K. Laaidi, A. Zeghnoun, E. Giraudet, P. Bretin, E. Mauri, and S. Vandentorren, 2010: Satellite monitoring of summer heat waves in the Paris metropolitan area. *Int. J. Climatol.*, **31**, 313–323, https://doi.org/10.1002/joc.2222.

Drouin, M. A., and Coauthors, 2022: raw2l1, v2.1.5b (commit 1876f233). Accessed 11 December 2023, https://gitlab.in2p3.fr/ipsl/sirta/raw2l1.

Dupont, E., L. Menut, B. Carissimo, J. Pelon, and P. Flamant, 1999: Comparison between the atmospheric boundary layer in Paris and its rural suburbs during the ECLAP experiment. *Atmos. Environ.*, **33**, 979–994, https://doi.org/10.1016/S1352-2310(98)00216-7.

DWD, 2019: Calculated daily values for different characteristic elements of soil and crops, version v19.3. Accessed 12 June 2023, https://opendata.dwd.de/climate_environment/CDC/derived_germany/soil/daily/historical/.

——, 2021: Historical heat warnings for Germany, version v001. Accessed 31 August 2023, https://opendata.dwd.de/climate_environment/health/historical_alerts/heat_warnings/.

——, 2022: Annual phenological statistics. Accessed 9 November 2023, https://www.dwd.de/DE/leistungen/phaeno_sta/phaenosta.html.

——, 2023a: Historical daily station observations (temperature, pressure, precipitation, sunshine duration, etc.) for Germany, version v23.3. Accessed 23 January 2024, https://opendata.dwd.de/climate_environment/CDC/observations_germany/climate/daily/kl/historical/.

——, 2023b: 10-minute station observations of air temperature for Germany, version v23.3. Accessed 12 December 2023, https://opendata.dwd.de/climate_environment/CDC/observations_germany/climate/10_minutes/air_temperature/historical/.

EEA, 2016: EU-DEM (raster) – Version 1.1. Accessed 30 May 2023, https://sdi.eea.europa.eu/catalogue/srv/api/records/3473589f-0854-4601-919e-2e7dd172ff50.

ESA, 2017: Land cover CCI: Product user guide version 1.1. Tech. Rep., 52 pp., https://climate.esa.int/media/documents/ESACCI-LC-Ph2-PUGv3_1.1.pdf.

Fenner, D., F. Meier, D. Scherer, and A. Polze, 2014: Spatial and temporal air temperature variability in Berlin, Germany, during the years 2001–2010. *Urban Climate*, **10**, 308–331, https://doi.org/10.1016/j.uclim.2014.02.004.

——, ——, B. Bechtel, M. Otto, and D. Scherer, 2017: Intra and inter 'local climate zone' variability of air temperature as observed by crowdsourced citizen weather stations in Berlin, Germany. *Meteor. Z.*, **26**, 525–547, https://doi.org/10.1127/metz/2017/0861.

——, A. Holtmann, F. Meier, I. Langer, and D. Scherer, 2019: Contrasting changes of urban heat island intensity during hot weather episodes. *Environ. Res. Lett.*, **14**, 124013, https://doi.org/10.1088/1748-9326/ab506b.

——, B. Bechtel, M. Demuzere, J. Kittner, and F. Meier, 2021: CrowdQC+ – A quality-control for crowdsourced air-temperature observations enabling world-wide urban climate applications. *Front. Environ. Sci.*, **9**, 720747, https://doi.org/10.3389/fenvs.2021.720747.

Fernando, H., 2010: Fluid dynamics of urban atmospheres in complex terrain. *Annu. Rev. Fluid Mech.*, **42**, 365–389, https://doi.org/10.1146/annurev-fluid-121108-145459.

Field, P. R., and Coauthors, 2023: Implementation of a double moment cloud microphysics scheme in the UK met office regional numerical weather prediction model. *Quart. J. Roy. Meteor. Soc.*, **149**, 703–739, https://doi.org/10.1002/qj.4414.

Finch, D. P., P. I. Palmer, and T. Zhang, 2022: Automated detection of atmospheric NO_2 plumes from satellite data: A tool to help infer anthropogenic combustion emissions. *Atmos. Meas. Tech.*, **15**, 721–733, https://doi.org/10.5194/amt-15-721-2022.

——, Ed., 2021: *Springer Handbook of Atmospheric Measurements.* Springer, 1748 pp., https://doi.org/10.1007/978-3-030-52171-4.

Gabriel, K. M., and W. R. Endlicher, 2011: Urban and rural mortality rates during heat waves in Berlin and Brandenburg, Germany. *Environ. Pollut.*, **159**, 2044–2050, https://doi.org/10.1016/j.envpol.2011.01.016.

Geiß, A., and Coauthors, 2017: Mixing layer height as an indicator for urban air quality? *Atmos. Meas. Tech.*, **10**, 2969–2988, https://doi.org/10.5194/amt-10-2969-2017.

GeoBasis-DE/BKG, 2021: Verwaltungsgebiete 1:250 000 mit Einwohnerzahlen. Accessed 14 December 2023, https://www.geoportal.de/map.html?map=tk_08-verwaltungsgebiete-1-250000.

GeoBasis-DE/LGB, 2022: Bildbasiertes Digitales Oberflächenmodell – bDOM. Accessed 13 December 2023, https://geobroker.geobasis-bb.de/gbss.php?MODE=GetProductInformation&PRODUCTID=41cc9969-8b70-4152-8c6f-812d457bcfe2.

——, 2023a: Amtliches Liegenschaftskatasterinformationssystem (ALKIS-Daten) Brandenburg. Accessed 13 December 2023, https://geobroker.geobasis-bb.de/gbss.php?MODE=GetProductInformation&PRODUCTID=6de36219-3e68-489e-8ebc-632e5ffb6dc9.

——, 2023b: Digitales Geländemodell – DGM. Accessed 13 December 2023, https://geobroker.geobasis-bb.de/gbss.php?MODE=GetProductInformation&PRODUCTID=518094b9-d294-4e99-aeb2-550592a00682.

Geoportal Berlin, 2014: Straßenbefahrung 2014. Accessed 13 December 2023, https://fbinter.stadt-berlin.de/fb?loginkey=showMap&mapId=k_StraDa@senstadt.

——, 2021: DOM – Digitales Oberflächenmodell. Accessed 13 December 2023, https://fbinter.stadt-berlin.de/fb?loginkey=showMap&mapId=k_dom1@senstadt.

——, 2022a: Einwohnerdichte 2021 (Umweltatlas). Accessed 14 December 2023, https://fbinter.stadt-berlin.de/fb/index.jsp?loginkey=showMap&mapId=k_06_06ewdichte2021@senstadt.

——, 2022b: ATKIS DGM – Digitales Geländemodell. Accessed 13 December 2023, https://fbinter.stadt-berlin.de/fb?loginkey=showMap&mapId=k_dgm1@senstadt.

——, 2022c: Energieverbrauch – Fernwärme (Umweltatlas). Accessed 13 December 2023, https://fbinter.stadt-berlin.de/fb?loginkey=showMap&mapId=k_energieverbraeuche_ea_fw@senstadt.

——, 2023: ALKIS Berlin (Amtliches Liegenschaftskatasterinformationssystem). Accessed, 13 December 2023, https://fbinter.stadt-berlin.de/fb?loginkey=showMap&mapId=wmsk_alkis@senstadt.

Godowitch, J. M., J. K. S. Ching, and J. F. Clarke, 1985: Evolution of the nocturnal inversion layer at an urban and nonurban location. *J. Climate Appl. Meteor.*, **24**, 791–804, https://doi.org/10.1175/1520-0450(1985)024<0791:EOTNIL>2.0.CO;2.

——, ——, and ——, 1987: Spatial variation of the evolution and structure of the urban boundary layer. *Bound.-Layer Meteor.*, **38**, 249–272, https://doi.org/10.1007/BF00122447.

Gorelick, N., M. Hancher, M. Dixon, S. Ilyushchenko, D. Thau, and R. Moore, 2017: Google Earth Engine: Planetary-scale geospatial analysis for everyone. *Remote Sens. Environ.*, **202**, 18–27, https://doi.org/10.1016/j.rse.2017.06.031.

Grimmond, C. S. B., and Coauthors, 2010: Climate and more sustainable cities: Climate information for improved planning and management of cities (producers/capabilities perspective). *Procedia Environ. Sci.*, **1**, 247–274, https://doi.org/10.1016/j.proenv.2010.09.016.

——, and Coauthors, 2020: Integrated urban hydrometeorological, climate and environmental services: Concept, methodology and key messages. *Urban Climate*, **33**, 100623, https://doi.org/10.1016/j.uclim.2020.100623.

Hall, T. W., and Coauthors, 2024: Utility of thermal remote sensing for evaluation of a high-resolution weather model in a city. *Quart. J. Roy. Meteor. Soc.*, **150**, 1771–1790, https://doi.org/10.1002/qj.4669.

Heaviside, C., X.-M. Cai, and S. Vardoulakis, 2015: The effects of horizontal advection on the urban heat island in Birmingham and the West Midlands, United

Kingdom during a heatwave. *Quart. J. Roy. Meteor. Soc.*, **141**, 1429–1441, https://doi.org/10.1002/qj.2452.

Hersbach, H., and Coauthors, 2023: ERA5 hourly data on single levels from 1940 to present. Copernicus Climate Change Service (C3S) Climate Data Store (CDS), accessed 22 June 2023, https://doi.org/10.24381/cds.adbb2d47.

Hertwig, D., and Coauthors, 2020: Urban signals in high-resolution weather and climate simulations: Role of urban land-surface characterisation. *Theor. Appl. Climatol.*, **142**, 701–728, https://doi.org/10.1007/s00704-020-03294-1.

——, C. S. B. Grimmond, S. Kotthaus, C. Vanderwel, H. Gough, M. Haeffelin, and A. Robins, 2021: Variability of physical meteorology in urban areas at different scales: Implications for air quality. *Faraday Discuss.*, **226**, 149–172, https://doi.org/10.1039/D0FD00098A.

——, M. McGrory, M. Paskin, Y. Liu, S. Lo Piano, H. Llanwarne, S. T. Smith, and S. Grimmond, 2024: Multi-scale harmonisation Across Physical and Socio-Economic Characteristics of a City region (MAPSECC): London, UK. Zenodo, accessed 22 June 2024, https://doi.org/10.5281/zenodo.12190340.

Hervo, M., Y. Poltera, and A. Haefele, 2016: An empirical method to correct for temperature-dependent variations in the overlap function of CHM15k ceilometers. *Atmos. Meas. Tech.*, **9**, 2947–2959, https://doi.org/10.5194/amt-9-2947-2016.

Hildebrand, P. H., and B. Ackerman, 1984: Urban effects on the convective boundary layer. *J. Atmos. Sci.*, **41**, 76–91, https://doi.org/10.1175/1520-0469(1984)041<0076:UEOTCB>2.0.CO;2.

Ho, H. C., K. K.-L. Lau, C. Ren, and E. Ng, 2017: Characterizing prolonged heat effects on mortality in a sub-tropical high-density city, Hong Kong. *Int. J. Biometeorol.*, **61**, 1935–1944, https://doi.org/10.1007/s00484-017-1383-4.

Hohenegger, C., and Coauthors, 2023: FESSTVaL: The field experiment on submesoscale spatio-temporal variability in Lindenberg. *Bull. Amer. Meteor. Soc.*, **104**, E1875–E1892, https://doi.org/10.1175/BAMS-D-21-0330.1.

Holzworth, G. C., 1964: Estimates of mean maximum mixing depths in the contiguous United States. *Mon. Wea. Rev.*, **92**, 235–242, https://doi.org/10.1175/1520-0493(1964)092<0235:EOMMMD>2.3.CO;2.

Horbert, M., A. Kirchgeorg, and A. von Stülpnagel, 1984: On the method for charting the climate of an entire large urban area. *Energy Build.*, **7**, 109–116, https://doi.org/10.1016/0378-7788(84)90033-1.

Hu, X.-M., P. M. Klein, M. Xue, J. K. Lundquist, F. Zhang, and Y. Qi, 2013: Impact of low-level jets on the nocturnal urban heat island intensity in Oklahoma City. *J. Appl. Meteor. Climatol.*, **52**, 1779–1802, https://doi.org/10.1175/JAMC-D-12-0256.1.

Huang, M., Z. Gao, S. Miao, F. Chen, M. A. LeMone, J. Li, F. Hu, and L. Wang, 2017: Estimate of boundary-layer depth over Beijing, China, using Doppler lidar data during SURF-2015. *Bound.-Layer Meteor.*, **162**, 503–522, https://doi.org/10.1007/s10546-016-0205-2.

Hupfer, P., and F.-M. Chmielewski, 1990: *Das Klima von Berlin.* Akademie-Verlag, 288 pp.

Imhoff, M. L., P. Zhang, R. E. Wolfe, and L. Bounoua, 2010: Remote sensing of the urban heat island effect across biomes in the continental USA. *Remote Sens. Environ.*, **114**, 504–513, https://doi.org/10.1016/j.rse.2009.10.008.

Inoue, J., and K. Sato, 2023: Comparison of the depolarization measurement capability of a lidar ceilometer with cloud particle sensor sondes: A case study of liquid water clouds. *Polar Sci.*, **35**, 100911, https://doi.org/10.1016/j.polar.2022.100911.

IPCC, 2023: *Climate Change 2022: Impacts, Adaptation and Vulnerability.* H.-O. Pörtner et al., Eds., Cambridge University Press, 3056 pp., https://doi.org/10.1017/9781009325844.

Iqbal, N., and Coauthors, 2024: How does perceived heat stress differ between urban forms and human vulnerability profiles? – Case study Berlin. *EGUsphere*, https://doi.org/10.5194/egusphere-2024-1907, preprint.

Joe, P., and Coauthors, 2021: Guidance on integrated urban hydro-meteorological, climate and environmental services: Challenges and the way forward. *Urban Climate Science for Planning Healthy Cities*, C. Ren and G. McGregor, Eds., Springer, 311–338, https://doi.org/10.1007/978-3-030-87598-5_14.

Kallistratova, M., R. D. Kouznetsov, D. D. Kuznetsov, I. N. Kuznetsova, M. Nakhaev, and G. Chirokova, 2009: Summertime low-level jet characteristics measured by sodars over rural and urban areas. *Meteor. Z.*, **18**, 289–295, https://doi.org/10.1127/0941-2948/2009/0380.

Kljun, N., P. Calanca, M. W. Rotach, and H. P. Schmid, 2015: A simple two-dimensional parameterisation for Flux Footprint Prediction (FFP). *Geosci. Model Dev.*, **8**, 3695–3713, https://doi.org/10.5194/gmd-8-3695-2015.

——, ——, ——, and ——, 2023: A simple two-dimensional parameterisation for Flux Footprint Prediction (FFP). Accessed 11 December 2023, https://footprint.kljun.net/.

Klose, B., 2016: *Meteorologie: Eine interdisziplinäre Einführung in die Physik der Atmosphäre.* Springer, 524 pp., https://doi.org/10.1007/978-3-662-43622-6.

Kormann, R., and F. X. Meixner, 2001: An analytical footprint model for non-neutral stratification. *Bound.-Layer Meteor.*, **99**, 207–224, https://doi.org/10.1023/A:1018991015119.

Kotthaus, S., and C. S. B. Grimmond, 2014: Energy exchange in a dense urban environment – Part I: Temporal variability of long-term observations in central London. *Urban Climate*, **10**, 261–280, https://doi.org/10.1016/j.uclim.2013.10.002.

——, and ——, 2018a: Atmospheric boundary layer characteristics from ceilometer measurements Part 1: A new method to track mixed layer height and classify clouds. *Quart. J. Roy. Meteor. Soc.*, **144**, 1525–1538, https://doi.org/10.1002/qj.3299.

——, and ——, 2018b: Atmospheric boundary layer characteristics from ceilometer measurements Part 2: Application to London's urban boundary layer. *Quart. J. Roy. Meteor. Soc.*, **144**, 1511–1524, https://doi.org/10.1002/qj.3298.

——, E. O'Connor, C. Münkel, C. Charlton-Perez, M. Haeffelin, A. M. Gabey, and C. S. B. Grimmond, 2016: Recommendations for processing atmospheric attenuated backscatter profiles from Vaisala CL31 ceilometers. *Atmos. Meas. Tech.*, **9**, 3769–3791, https://doi.org/10.5194/amt-9-3769-2016.

——, C. H. Halios, J. F. Barlow, and C. S. B. Grimmond, 2018: Volume for pollution dispersion: London's atmospheric boundary layer during ClearfLo observed with two ground-based lidar types. *Atmos. Environ.*, **190**, 401–414, https://doi.org/10.1016/j.atmosenv.2018.06.042.

——, and Coauthors, 2020: Tailored algorithms for the detection of the atmospheric boundary layer height from common Automatic Lidars and Ceilometers (ALC). *Remote Sens.*, **12**, 3259, https://doi.org/10.3390/rs12193259.

——, and Coauthors, 2023a: Atmospheric boundary layer height from ground-based remote sensing: A review of capabilities and limitations. *Atmos. Meas. Tech.*, **16**, 433–479, https://doi.org/10.5194/amt-16-433-2023.

——, and Coauthors, 2023b: STRATfinder, branches "for_cl61" (commit fc5d5d6f) and "master" (commit be933d0c). Accessed 11 December 2023, https://gitlab.in2p3.fr/ipsl/sirta/mld/stratfinder/stratfinder.

Laaidi, K., A. Zeghnoun, B. Dousset, P. Bretin, S. Vandentorren, E. Giraudet, and P. Beaudeau, 2012: The impact of heat islands on mortality in Paris during the August 2003 heat wave. *Environ. Health Perspect.*, **120**, 254–259, https://doi.org/10.1289/ehp.1103532.

Lama, S., S. Houweling, K. F. Boersma, I. Aben, H. A. C. D. van der Gon, and M. C. Krol, 2022: Estimation of OH in urban plumes using TROPOMI-inferred NO_2/CO. *Atmos. Chem. Phys.*, **22**, 16 053–16 071, https://doi.org/10.5194/acp-22-16053-2022.

Lamer, K., and Coauthors, 2022: Going mobile to address emerging climate equity needs in the heterogeneous urban environment. *Bull. Amer. Meteor. Soc.*, **103**, E2069–E2080, https://doi.org/10.1175/BAMS-D-21-0336.1.

Langer, I., E. Fakharizadehshirazi, and J. Werner, 2021: Spatial variation of physiologically equivalent temperature in different Local Climate Zones of a large city during a hot spell. *Meteor. Z.*, **30**, 115–125, https://doi.org/10.1127/metz/2020/0996.

Lean, H. W., J. F. Barlow, and C. H. Halios, 2019: The impact of spin-up and resolution on the representation of a clear convective boundary layer over London in order 100 m grid-length versions of the Met Office Unified Model. *Quart. J. Roy. Meteor. Soc.*, **145**, 1674–1689, https://doi.org/10.1002/qj.3519.

——, ——, and P. A. Clark, 2022: The use of 100 m scale NWP models to understand differences between different measures of mixing height in a morning

growing clear convective boundary layer over London. *Quart. J. Roy. Meteor. Soc.*, **148**, 1983–1995, https://doi.org/10.1002/qj.4291.

Levelt, P. F., and Coauthors, 2022: Air quality impact of COVID-19 lockdown measures detected from space using high spatial resolution observations of multiple trace gases from Sentinel-5P/TROPOMI. *Atmos. Chem. Phys.*, **22**, 10 319–10 351, https://doi.org/10.5194/acp-22-10319-2022.

LI-COR, 2022: EddyPro Software. LI-COR, https://www.licor.com/env/support/EddyPro/topics/whats-new.html.

Liu, Y., Z. Luo, and S. Grimmond, 2022: Revising the definition of anthropogenic heat flux from buildings: Role of human activities and building storage heat flux. *Atmos. Chem. Phys.*, **22**, 4721–4735, https://doi.org/10.5194/acp-22-4721-2022.

——, ——, and ——, 2023: Impact of building envelope design parameters on diurnal building anthropogenic heat emission. *Build. Environ.*, **234**, 110134, https://doi.org/10.1016/j.buildenv.2023.110134.

Lorente, A., and Coauthors, 2019: Quantification of nitrogen oxides emissions from build-up of pollution over Paris with TROPOMI. *Sci. Rep.*, **9**, 20033, https://doi.org/10.1038/s41598-019-56428-5.

Lorenz, J. M., R. Kronenberg, C. Bernhofer, and D. Niyogi, 2019: Urban rainfall modification: Observational climatology over Berlin, Germany. *J. Geophys. Res. Atmos.*, **124**, 731–746, https://doi.org/10.1029/2018JD028858.

Loridan, T., F. Lindberg, O. Jorba, S. Kotthaus, S. Grossman-Clarke, and C. S. B. Grimmond, 2013: High resolution simulation of the variability of surface energy balance fluxes across central London with urban zones for energy partitioning. *Bound.-Layer Meteor.*, **147**, 493–523, https://doi.org/10.1007/s10546-013-9797-y.

Lotteraner, C., and M. Piringer, 2016: Mixing-height time series from operational ceilometer aerosol-layer heights. *Bound.-Layer Meteor.*, **161**, 265–287, https://doi.org/10.1007/s10546-016-0169-2.

Lowry, W. P., 1977: Empirical estimation of urban effects on climate: A problem analysis. *J. Appl. Meteor.*, **16**, 129–135, https://doi.org/10.1175/1520-0450(1977)016<0129:EEOUEO>2.0.CO;2.

Lyapustin, A., and Y. Wang, 2018: MCD19A2 MODIS/Terra+Aqua land aerosol optical depth daily L2G Global 1km SIN Grid V006. NASA EOSDIS Land Processes Distributed Active Archive Center, accessed 13 April 2023, https://doi.org/10.5067/MODIS/MCD19A2.006.

Manninen, A. J., E. J. O'Connor, V. Vakkari, and T. Petäjä, 2016: A generalised background correction algorithm for a Halo Doppler lidar and its application to data from Finland. *Atmos. Meas. Tech.*, **9**, 817–827, https://doi.org/10.5194/amt-9-817-2016.

——, and Coauthors, 2023: HALO lidar toolbox (commit 3bb58de). Accessed 18 December 2023, https://github.com/manninenaj/HALO_lidar_toolbox.

Manoli, G., S. Fatichi, E. Bou-Zeid, and G. G. Katul, 2020: Seasonal hysteresis of surface urban heat islands. *Proc. Natl. Acad. Sci. USA*, **117**, 7082–7089, https://doi.org/10.1073/pnas.1917554117.

Marconcini, M., A. Metz-Marconcini, T. Esch, and N. Gorelick, 2021: Understanding current trends in Global Urbanisation – The World Settlement Footprint Suite. GI_Forum 2021, 6 pp., https://austriaca.at/0xc1aa5576%200x003c9b4c.pdf.

Masson, V., and Coauthors, 2008: The Canopy and Aerosol Particles Interactions in TOulouse Urban Layer (CAPITOUL) experiment. *Meteor. Atmos. Phys.*, **102**, 135–157, https://doi.org/10.1007/s00703-008-0289-4.

——, A. Lemonsu, J. Hidalgo, and J. Voogt, 2020: Urban climates and climate change. *Annu. Rev. Environ. Resour.*, **45**, 411–444, https://doi.org/10.1146/annurev-environ-012320-083623.

Mauder, M., and T. Foken, 2004: Documentation and instruction manual of the eddy covariance software package TK2. Universität Bayreuth, Abt. Mikrometeorologie, Arbeitsergebnisse No. 26, 45 pp., https://epub.uni-bayreuth.de/id/eprint/884/1/ARBERG026.pdf.

McGrory, M., and Coauthors, 2024: urbisphere_presentations_UR-3: Dynamic Anthropogenic actiVities and feedback to Emissions (DAVE): An agent-based model for heat and exposure to other anthropogenic emissions. Zenodo, accessed 2 April 2024, https://doi.org/10.5281/zenodo.10889900.

Mestayer, P., and Coauthors, 2005: The urban boundary-layer field campaign in Marseille (UBL/CLU-ESCOMPTE): Set-up and first results. *Bound.-Layer Meteor.*, **114**, 315–365, https://doi.org/10.1007/s10546-004-9241-4.

Muller, C. L., L. Chapman, C. S. B. Grimmond, D. T. Young, and X. Cai, 2013: Sensors and the city: A review of urban meteorological networks. *Int. J. Climatol.*, **33**, 1585–1600, https://doi.org/10.1002/joc.3678.

Müller, I., T. Erbertseder, and H. Taubenböck, 2022: Tropospheric NO_2: Explorative analyses of spatial variability and impact factors. *Remote Sens. Environ.*, **270**, 112839, https://doi.org/10.1016/j.rse.2021.112839.

Nazarian, N., and Coauthors, 2022: Integrated assessment of urban overheating impacts on human life. *Earth's Future*, **10**, e2022EF002682, https://doi.org/10.1029/2022EF002682.

Netatmo, 2023: Netatmo smart home weather station. Accessed 11 December 2023, https://www.netatmo.com/smart-weather-station.

Newsom, R. K., W. A. Brewer, J. M. Wilczak, D. E. Wolfe, S. P. Oncley, and J. K. Lundquist, 2017: Validating precision estimates in horizontal wind measurements from a Doppler lidar. *Atmos. Meas. Tech.*, **10**, 1229–1240, https://doi.org/10.5194/amt-10-1229-2017.

Nicolini, G., and Coauthors, 2022: Direct observations of CO_2 emission reductions due to COVID-19 lockdown across European urban districts. *Sci. Total Environ.*, **830**, 154662, https://doi.org/10.1016/j.scitotenv.2022.154662.

Offerle, B., C. S. B. Grimmond, K. Fortuniak, and W. Pawlak, 2006: Intraurban differences of surface energy fluxes in a central European city. *J. Appl. Meteor. Climatol.*, **45**, 125–136, https://doi.org/10.1175/JAM2319.1.

Oke, T. R., 1981: Canyon geometry and the nocturnal urban heat island: Comparison of scale model and field observations. *J. Climatol.*, **1**, 237–254, https://doi.org/10.1002/joc.3370010304.

——, and C. East, 1971: The urban boundary layer in Montreal. *Bound.-Layer Meteor.*, **1**, 411–437, https://doi.org/10.1007/BF00184781.

Pal, S., and Coauthors, 2012: Spatio-temporal variability of the atmospheric boundary layer depth over the Paris agglomeration: An assessment of the impact of the urban heat island intensity. *Atmos. Environ.*, **63**, 261–275, https://doi.org/10.1016/j.atmosenv.2012.09.046.

Päschke, E., R. Leinweber, and V. Lehmann, 2015: An assessment of the performance of a 1.5 µm Doppler lidar for operational vertical wind profiling based on a 1-year trial. *Atmos. Meas. Tech.*, **8**, 2251–2266, https://doi.org/10.5194/amt-8-2251-2015.

Peng, J., and Coauthors, 2017: Ceilometer-based analysis of Shanghai's boundary layer height (under rain- and fog-free conditions). *J. Atmos. Oceanic Technol.*, **34**, 749–764, https://doi.org/10.1175/JTECH-D-16-0132.1.

Peng, S., and Coauthors, 2012: Surface urban heat island across 419 global big cities. *Environ. Sci. Technol.*, **46**, 696–703, https://doi.org/10.1021/es2030438.

Perlewitz, P., 1890: Über den Einfluss der Stadt Berlin auf deren klimatische Verhältnisse. *Das Wetter*, **6**, 97–109.

Porson, A., P. A. Clark, I. N. Harman, M. J. Best, and S. E. Belcher, 2010a: Implementation of a new urban energy budget scheme in the MetUM. Part I: Description and idealized simulations. *Quart. J. Roy. Meteor. Soc.*, **136**, 1514–1529, https://doi.org/10.1002/qj.668.

——, ——, ——, ——, and ——, 2010b: Implementation of a new urban energy budget scheme into MetUM. Part II: Validation against observations and model intercomparison. *Quart. J. Roy. Meteor. Soc.*, **136**, 1530–1542, https://doi.org/10.1002/qj.572.

Ronda, R. J., G.-J. Steeneveld, and B. G. Heusinkveld, 2017: Urban fine-scale forecasting reveals weather conditions with unprecedented detail. *Bull. Amer. Meteor. Soc.*, **98**, 2675–2688, https://doi.org/10.1175/BAMS-D-16-0297.1.

Rotach, M. W., and Coauthors, 2005: BUBBLE – An urban boundary layer meteorology project. *Theor. Appl. Climatol.*, **81**, 231–261, https://doi.org/10.1007/s00704-004-0117-9.

Saénz, J., S. J. González-Rojí, S. Carreno-Madinabeitia, and G. Ibarra-Berastegi, 2018: aiRthermo: Atmospheric Thermodynamics and Visualization, v1.2.1. Accessed 12 December 2023, https://cran.r-project.org/package=aiRthermo.

Santanello, J. A., M. A. Friedl, and W. P. Kustas, 2005: An empirical investigation of convective planetary boundary layer evolution and its relationship with the land surface. *J. Appl. Meteor.*, **44**, 917–932, https://doi.org/10.1175/JAM2240.1.

Saunders, B., S. Grimmond, D. Hertwig, S. I. Bohnenstengel, H. W. Lean, and W. Morrison, 2024: Methodology to evaluate numerical weather predictions using large aperture scintillometry sensible heat fluxes: Demonstration in London. *Quart. J. Roy. Meteor. Soc.*, https://doi.org/10.1002/qj.4837, in press.

Schatke, M., F. Meier, B. Schröder, and S. Weber, 2022: Impact of the 2020 COVID-19 lockdown on NO_2 and PM_{10} concentrations in Berlin, Germany. *Atmos. Environ.*, **290**, 119372, https://doi.org/10.1016/j.atmosenv.2022.119372.

Scherer, D., U. Fehrenbach, T. Lakes, S. Lauf, F. Meier, and C. Schuster, 2014: Quantification of heat-stress related mortality hazard, vulnerability and risk in Berlin, Germany. *Die Erde*, **144**, 238–259, https://doi.org/10.12854/erde-144-17.

——, and Coauthors, 2019a: Urban climate under change [UC]2 – A national research programme for developing a building-resolving atmospheric model for entire city regions. *Meteor. Z.*, **28**, 95–104, https://doi.org/10.1127/metz/2019/0913.

——, F. Ament, S. Emeis, U. Fehrenbach, B. Leitl, K. Scherber, C. Schneider, and U. Vogt, 2019b: Three-dimensional observation of atmospheric processes in cities. *Meteor. Z.*, **28**, 121–138, https://doi.org/10.1127/metz/2019/0911.

Schneider, C., B. Neuwirth, S. Schneider, D. Balanzategui, S. Elsholz, D. Fenner, F. Meier, and I. Heinrich, 2022: Using the dendro-climatological signal of urban trees as a measure of urbanization and urban heat island. *Urban Ecosyst.*, **25**, 849–865, https://doi.org/10.1007/s11252-021-01196-2.

Seibert, P., F. Beyrich, S.-E. Gryning, S. Joffre, A. Rasmussen, and P. Tercier, 2000: Review and intercomparison of operational methods for the determination of the mixing height. *Atmos. Environ.*, **34**, 1001–1027, https://doi.org/10.1016/S1352-2310(99)00349-0.

Shi, Z., and Coauthors, 2019: Introduction to the special issue "In-depth study of air pollution sources and processes within Beijing and its surrounding region (APHH-Beijing)". *Atmos. Chem. Phys.*, **19**, 7519–7546, https://doi.org/10.5194/acp-19-7519-2019.

Simón-Moral, A., A. Dipankar, M. Roth, C. Sánchez, E. Velasco, and X. Huang, 2019: Application of MORUSES single-layer urban canopy model in a tropical city: Results from Singapore. *Quart. J. Roy. Meteor. Soc.*, **146**, 576–597, https://doi.org/10.1002/qj.3694.

Sismanidis, P., B. Bechtel, M. Perry, and D. Ghent, 2022: The seasonality of surface urban heat islands across climates. *Remote Sens.*, **14**, 2318, https://doi.org/10.3390/rs14102318.

Sparv, 2019: Windsond Product Catalogue. Accessed 12 December 2023, https://files.sparvembedded.com/windsond_catalog_Feb2019.pdf.

StatBB, 2021: Brandenburg population data (2021). Amt für Statistik Berlin-Brandenburg, accessed 11 Sep 2024, https://download.statistik-berlin-brandenburg.de/f9096e7495a98683/2c8cb569f8e6/bevoelkerungsstand-lange-reihe.xlsx.

Stewart, I. D., and T. R. Oke, 2012: Local climate zones for urban temperature studies. *Bull. Amer. Meteor. Soc.*, **93**, 1879–1900, https://doi.org/10.1175/BAMS-D-11-00019.1.

Storch, T., and Coauthors, 2023: The EnMAP imaging spectroscopy mission towards operations. *Remote Sens. Environ.*, **294**, 113632, https://doi.org/10.1016/j.rse.2023.113632.

Straaten, A., and S. Weber, 2021: Measurement report: Three years of size-resolved eddy-covariance particle number flux measurements in an urban environment. *Atmos. Chem. Phys.*, **21**, 18 707–18 726, https://doi.org/10.5194/acp-21-18707-2021.

——, F. Meier, D. Scherer, and S. Weber, 2022: Significant reduction of ultrafine particle emission fluxes to the urban atmosphere during the COVID-19 lockdown. *Sci. Total Environ.*, **838**, 156516, https://doi.org/10.1016/j.scitotenv.2022.156516.

Sulzer, M., and A. Christen, 2024: Climate projections of human thermal comfort for indoor workplaces. *Climatic Change*, **177**, 28, https://doi.org/10.1007/s10584-024-03685-7.

Tack, F., and Coauthors, 2019: Intercomparison of four airborne imaging DOAS systems for tropospheric NO_2 mapping – The AROMAPEX campaign. *Atmos. Meas. Tech.*, **12**, 211–236, https://doi.org/10.5194/amt-12-211-2019.

Tapper, N., 1990: Urban influences on boundary layer temperature and humidity: Results from Christchurch, New Zealand. *Atmos. Environ.*, **24**, 19–27, https://doi.org/10.1016/0957-1272(90)90005-F.

Theeuwes, N. E., J. F. Barlow, A. J. Teuling, C. S. B. Grimmond, and S. Kotthaus, 2019: Persistent cloud cover over mega-cities linked to surface heat release. *npj Climate Atmos. Sci.*, **2**, 15, https://doi.org/10.1038/s41612-019-0072-x.

Thiermann, V., and H. Grassl, 1992: The measurement of turbulent surface-layer fluxes by use of bichromatic scintillation. *Bound.-Layer Meteor.*, **58**, 367–389, https://doi.org/10.1007/BF00120238.

Toth, C., and G. Jóźków, 2016: Remote sensing platforms and sensors: A survey. *ISPRS J. Photogramm. Remote Sens.*, **115**, 22–36, https://doi.org/10.1016/j.isprsjprs.2015.10.004.

Tsiringakis, A., N. E. Theeuwes, J. F. Barlow, and G.-J. Steeneveld, 2022: Interactions between the nocturnal low-level jets and the urban boundary layer: A case study over London. *Bound.-Layer Meteor.*, **183**, 249–272, https://doi.org/10.1007/s10546-021-00681-7.

Tuholske, C., K. Caylor, C. Funk, A. Verdin, S. Sweeney, K. Grace, P. Peterson, and T. Evans, 2021: Global urban population exposure to extreme heat. *Proc. Natl. Acad. Sci. USA*, **118**, e2024792118, https://doi.org/10.1073/pnas.2024792118.

Vakkari, V., A. J. Manninen, E. J. O'Connor, J. H. Schween, P. G. van Zyl, and E. Marinou, 2019: A novel post-processing algorithm for Halo Doppler lidars. *Atmos. Meas. Tech.*, **12**, 839–852, https://doi.org/10.5194/amt-12-839-2019.

Van Hove, M., and Coauthors, 2023a: Overlap_corr (commit 033e6c95). Accessed 11 December 2023, https://gitlab.in2p3.fr/ipsl/sirta/chm15k/overlap_corr.

——, and Coauthors, 2023b: QC STRAFINDER (commit ea6b34a1). Accessed 11 December 2023, https://gitlab.in2p3.fr/ipsl/sirta/mld/stratfinder/qc-sf-python.

Van Kesteren, B., F. Beyrich, O. K. Hartogensis, and M. Braam, 2015: Long-term evaluation of the Scintec boundary-layer scintillometer and the Wageningen large-aperture scintillometer: Implications for scintillometer users. *Bound.-Layer Meteor.*, **156**, 303–323, https://doi.org/10.1007/s10546-015-0023-y.

Van Weverberg, K., C. J. Morcrette, I. Boutle, K. Furtado, and P. R. Field, 2021a: A bimodal diagnostic cloud fraction parameterization. Part I: Motivating analysis and scheme description. *Mon. Wea. Rev.*, **149**, 841–857, https://doi.org/10.1175/MWR-D-20-0224.1.

——, ——, and ——, 2021b: A bimodal diagnostic cloud fraction parameterization. Part II: Evaluation and resolution sensitivity. *Mon. Wea. Rev.*, **149**, 859–878, https://doi.org/10.1175/MWR-D-20-0230.1.

Varentsov, M., H. Wouters, V. Platonov, and P. Konstantinov, 2018: Megacity-induced mesoclimatic effects in the lower atmosphere: A modeling study for multiple summers over Moscow, Russia. *Atmosphere*, **9**, 50, https://doi.org/10.3390/atmos9020050.

Varentsov, M. I., D. Fenner, F. Meier, T. E. Samsonov, and M. Demuzere, 2021: Quantifying local- and meso-scale drivers of Moscow's urban heat island with reference and crowdsourced observations. *Front. Environ. Sci.*, **9**, 716968, https://doi.org/10.3389/fenvs.2021.716968.

Varquez, A. C. G., S. Kiyomoto, D. N. Khanh, and M. Kanda, 2021: Global 1-km present and future hourly anthropogenic heat flux. *Sci. Data*, **8**, 64, https://doi.org/10.1038/s41597-021-00850-w.

Veefkind, J., and Coauthors, 2012: TROPOMI on the ESA Sentinel-5 Precursor: A GMES mission for global observations of the atmospheric composition for climate, air quality and ozone layer applications. *Remote Sens. Environ.*, **120**, 70–83, https://doi.org/10.1016/j.rse.2011.09.027.

Vo, T. T., L. Hu, L. Xue, Q. Li, and S. Chen, 2023: Urban effects on local cloud patterns. *Proc. Natl. Acad. Sci. USA*, **120**, e2216765120, https://doi.org/10.1073/pnas.2216765120.

Vulova, S., F. Meier, A. D. Rocha, J. Quanz, H. Nouri, and B. Kleinschmit, 2021: Modeling urban evapotranspiration using remote sensing, flux footprints, and

artificial intelligence. *Sci. Total Environ.*, **786**, 147293, https://doi.org/10.1016/j.scitotenv.2021.147293.

Walters, D., and Coauthors, 2019: The Met Office Unified Model Global Atmosphere 7.0/7.1 and JULES Global Land 7.0 configurations. *Geosci. Model Dev.*, **12**, 1909–1963, https://doi.org/10.5194/gmd-12-1909-2019.

Wan, Z., 2019: Collection-6 MODIS land surface temperature products users' guide. 37 pp., https://lpdaac.usgs.gov/documents/715/MOD11_User_Guide_V61.pdf.

——, S. Hook, and G. Hulley, 2021: MODIS/Terra Land Surface Temperature/Emissivity 5-Min L2 Swath 1km V061. NASA EOSDIS Land Processes Distributed Active Archive Center, accessed 18 December 2023, https://doi.org/10.5067/MODIS/MOD11_L2.061.

Wang, J., A. Ma, Y. Zhong, Z. Zheng, and L. Zhang, 2022: Cross-sensor domain adaptation for high spatial resolution urban land-cover mapping: From airborne to spaceborne imagery. *Remote Sens. Environ.*, **277**, 113058, https://doi.org/10.1016/j.rse.2022.113058.

Wang, L., and D. Li, 2019: Modulation of the urban boundary layer heat budget by a heat wave. *Quart. J. Roy. Meteor. Soc.*, **145**, 1814–1831, https://doi.org/10.1002/qj.3526.

Wang, Y., C. L. Klipp, D. M. Garvey, D. A. Ligon, C. C. Williamson, S. S. Chang, R. K. Newsom, and R. Calhoun, 2007: Nocturnal low-level-jet-dominated atmospheric boundary layer observed by a Doppler lidar over Oklahoma City during JU2003. *J. Appl. Meteor. Climatol.*, **46**, 2098–2109, https://doi.org/10.1175/2006JAMC1283.1.

Ward, H. C., J. G. Evans, and C. S. B. Grimmond, 2014: Multi-scale sensible heat fluxes in the suburban environment from large-aperture scintillometry and eddy covariance. *Bound.-Layer Meteor.*, **152**, 65–89, https://doi.org/10.1007/s10546-014-9916-4.

——, S. Kotthaus, L. Järvi, and C. S. B. Grimmond, 2016: Surface urban energy and water balance scheme (SUEWS): Development and evaluation at two UK sites. *Urban Climate*, **18**, 1–32, https://doi.org/10.1016/j.uclim.2016.05.001.

Wiegner, M., and A. Geiß, 2012: Aerosol profiling with the Jenoptik ceilometer CHM15kx. *Atmos. Meas. Tech.*, **5**, 1953–1964, https://doi.org/10.5194/amt-5-1953-2012.

——, ——, I. Mattis, F. Meier, and T. Ruhtz, 2020: On the spatial variability of the regional aerosol distribution as determined from ceilometers. *Atmos. Chem. Phys. Discuss.*, https://doi.org/10.5194/acp-2020-332, preprint.

WMO, 2019: Guidance on integrated urban hydrometeorological, climate and environmental services – Volume I: Concept and methodology. WMO-1234, 52 pp., https://library.wmo.int/idurl/4/56760.

——, 2021: Guidance on integrated urban hydrometeorological, climate and environment services – Volume II: Demonstration cities. WMO-1234, 166 pp., https://library.wmo.int/idurl/4/57316.

Wood, C. R., and Coauthors, 2013: An overview of the urban boundary layer atmosphere network in Helsinki. *Bull. Amer. Meteor. Soc.*, **94**, 1675–1690, https://doi.org/10.1175/BAMS-D-12-00146.1.

Wood, N., and Coauthors, 2014: An inherently mass-conserving semi-implicit semi-Lagrangian discretization of the deep-atmosphere global non-hydrostatic equations. *Quart. J. Roy. Meteor. Soc.*, **140**, 1505–1520, https://doi.org/10.1002/qj.2235.

Xie, X., Z. Luo, S. Grimmond, and T. Sun, 2023: Impact of building density on natural ventilation potential and cooling energy saving across Chinese climate zones. *Build. Environ.*, **244**, 110621, https://doi.org/10.1016/j.buildenv.2023.110621.

Yue, M., M. Wang, J. Guo, H. Zhang, X. Dong, and Y. Liu, 2021: Long-term trend comparison of planetary boundary layer height in observations and CMIP6 models over China. *J. Climate*, **34**, 8237–8256, https://doi.org/10.1175/JCLI-D-20-1000.1.

Zanaga, D., and Coauthors, 2022: ESA WorldCover 10 m 2021 v200. Accessed 13 December 2023, https://doi.org/10.5281/zenodo.7254221.

Zeeman, M., C. C. Holst, M. Kossmann, D. Leukauf, C. Münkel, A. Philipp, R. Rinke, and S. Emeis, 2022: Urban atmospheric boundary-layer structure in complex topography: An empirical 3D case study for Stuttgart, Germany. *Front. Earth Sci.*, **10**, 840112, https://doi.org/10.3389/feart.2022.840112.

——, A. Christen, S. Grimmond, D. Fenner, W. Morrison, G. Feigel, M. Sulzer, and N. Chrysoulakis, 2024: Modular approach to near-time data management for multi-city atmospheric environmental observation campaigns. *EGUsphere*, https://doi.org/10.5194/egusphere-2024-1469, preprint.

Zhang, Y., L. Wang, J. A. Santanello, Z. Pan, Z. Gao, and D. Li, 2020: Aircraft observed diurnal variations of the planetary boundary layer under heat waves. *Atmos. Res.*, **235**, 104801, https://doi.org/10.1016/j.atmosres.2019.104801.

Zheng, Q., K. C. Seto, Y. Zhou, S. You, and Q. Weng, 2023: Nighttime light remote sensing for urban applications: Progress, challenges, and prospects. *ISPRS J. Photogramm. Remote Sens.*, **202**, 125–141, https://doi.org/10.1016/j.isprsjprs.2023.05.028.

Zhong, Y., B. Yan, J. Yi, R. Yang, M. Xu, Y. Su, Z. Zheng, and L. Zhang, 2023: Global urban high-resolution land-use mapping: From benchmarks to multi-megacity applications. *Remote Sens. Environ.*, **298**, 113758, https://doi.org/10.1016/j.rse.2023.113758.